THE ASTROPHYSICAL JOURNAL SUPPLEMENT SERIES, 103:41–62, 1996 March

THE PEAK-PATCH PICTURE OF COSMIC CATALOGS. II. VALIDATION

J. R. BOND
CIAR Cosmology Program, Canadian Institute for Theoretical Astrophysics, McLennan Physical Laboratories, Toronto, ONT M5S 1A1, Canada
AND
S. T. MYERS
Department of Astronomy, 105-24, California Institute of Technology, Pasadena, CA 91125; David Rittenhouse Laboratory, University of Pennsylvania, 209 S. 33d Street, Philadelphia, PA 19104-6396
Received 1993 August 2; accepted 1995 June 16

ABSTRACT

We compare hierarchical peak-patch catalogs with groups and clusters constructed using Couchman's adaptive P^3M simulations of a "standard" CDM model with amplitude parameter $\sigma_8 \approx 1$. The N-body groups are found using an identification algorithm based on average cluster overdensity and the peak-patch properties were determined using algorithms from Paper I. We show that the best agreement is obtained if we use (1) density peaks rather than shear eigenvalue peaks as candidate points, (2) ellipsoidal rather than spherical collapse dynamics, thereby including external tidal effects, and (3) a binary reduction method as opposed to a full exclusion method for solving the cloud-in-cloud problem of peak theory. These are also the best choices physically. The mass and internal energy distributions of the peaks and groups are quite similar, but the group kinetic energy distribution is offset by $\sim$12% in velocity dispersion, reflecting our finding that the N-body clusters are invariably out of isolated virial equilibrium. Individual peak-to-group comparisons show good agreement for high-mass, tightly bound groups, with growing scatter for lower masses and looser binding. The final state (Eulerian) spatial distribution of peak patches and N-body clusters are shown to be satisfyingly close. There is indication for the necessity of a small nonlinear correction to the Zeldovich peak velocities.

Subject headings: catalogs — cosmology: theory — galaxies: clusters: general — galaxies: formation — methods: numerical

1. INTRODUCTION

The hierarchical peak-patch picture is a way to generate point processes associated with deep gravitational potential wells which is more physically correct than the original single-filter snapshot of density peaks (Bardeen et al. 1986, hereafter BBKS). Not only can one now obtain cosmic mass and velocity functions, unlike the single-filter peaks theory, but the spatial correlation structure is also automatically included, including both statistical clustering of the peak patches as well as dynamical clustering via an adaptive Zeldovich approximation. The peak-patch picture can also be thought of as *the* physically logical development of the excursion set (Press-Schechter) approach: objects are treated as coherent extended entities rather than as disconnected bits of space. Algorithms for implementing hierarchical peak-patch simulations were described in Bond & Myers (1995a, hereafter BM1). We show how far one can go analytically and semi-analytically in calculating peak-patch mass and velocity functions and two-point correlation functions in Bond & Myers (1995c, hereafter BM4).

But does the technique work? If so, is it useful? In this paper we address the first question by making a detailed comparison of a peak-patch catalog with an N-body group catalog, both constructed from the same realization of initial conditions (§ 2). The theory is a (standard) adiabatic cold dark matter model with Gaussian scale-invariant initial conditions (density spectrum index $n_s = 1$), Hubble parameter $h = 0.5$, where $H_0 = 100\ h$ km s^{-1} Mpc^{-1}, and $\Omega_{\rm cdm} = 1$. The parameter defining the overall normalization amplitude for the model, σ_8, is needed to complete the specification of the theory. It is the relative rms fluctuation level of the mass enclosed within a sphere of radius 8 h^{-1} Mpc, calculated in linear perturbation theory, and evaluated at the current time. Our comparison N-body simulation, kindly provided by Hugh Couchman (Couchman 1991), was an adaptive P^3M simulation of a periodic box of comoving volume $(200\ h^{-1}\ \mathrm{Mpc})^3$, using 128^3 particles perturbed from an initial 128^3 grid. The amplitude of the simulation was $\sigma_8 = 0.97$. The objects in the N-body catalog are therefore clusters and groups. In § 2.1, we describe the group-finding algorithm we use to identify the clusters based on truncating the particle content of a group once a *volume*-averaged density threshold has been reached. We contrast this with the more standard friends-of-friends algorithm, which may be interpreted as truncating particle content once a smoothed *surface* density threshold has been reached.

The overall "bias factor" for the CDM spectrum we use for comparison, $b_8 \equiv \sigma_8^{-1} = 1.03$ is a relatively low one, hence a substantial amount of nonlinear dynamics is expected within the simulation volume. To match the cluster distribution will therefore be quite a challenge for a theory based upon simplified dynamical models acting on the initial conditions: higher biasing factors are much easier for us to match. We compare mass and velocity dispersion functions of the groups and the peaks in §§ 3.1–3.2. We make a direct peak-to-group comparison in § 3.3 and show visually how close the clustering patterns match in § 3.4.

We believe the reader will find the matching sufficiently impressive—especially for high-mass peak patches—to feel that the results we derive from the construction of catalogs of clusters which cover much larger volumes of space are as quantitatively accurate as could be obtained with a low-resolution N-body code if it could cover such huge volumes. This includes the reproduction of clustering patterns. Indeed perhaps we are more accurate since we automatically include the often important effect of evolution of the clusters across the simulation volume which is most often ignored in N-body simulations of clusters. These aspects of our method are described in Bond & Myers (1995b), hereafter BM3.

2. COMPARISON OF N-BODY GROUPS WITH HIERARCHICAL PEAK PATCHES

To establish whether the peak-patch method can accurately locate and measure the regions of collapsed structures, we compare a catalog of groups and clusters that we construct using the hierarchical peaks method with a catalog constructed from an N-body simulation. We start from exactly the same realization of initial conditions in a 128^3 box of length 200 h^{-1} Mpc. The N-body solution was computed by Hugh Couchman with his adaptive P^{3}M algorithm (Couchman 1991), using 128^3 particles. His calculation began with Zeldovich approximation displacements from the lattice sites at a redshift of 16 and evolved to $z_{\rm box} = 0$. The peaks were found on the 128^3 lattice. Since the P^{3}M output is for a uniform redshift, we set $z_{\rm pk} = z_{\rm box}$; i.e., evolution across the box for this comparison is turned off. The theoretical model was a "standard" adiabatic cold dark matter model with $\Omega_{\rm cdm} = 1$ and Hubble parameter $h = 0.5$. The transfer function for the density power-spectrum is the one given in Appendix G of BBKS. The normalizing amplitude was $\sigma_8 = 0.97$ (bias factor $b_8 = 1.03$). Such a low bias is quite a challenge for our method since the amount of dynamics is quite large compared with higher bias models.

The Couchman P^{3}M simulation was analyzed using a novel group finding algorithm based on average overdensities described below in § 2.1 and in Appendix A. The implementation of the hierarchical peaks method was described in BM1. One-point number density distributions for mass and internal binding energy of the peaks and P^{3}M groups are compared in § 3 to show how the various options in the peak algorithm fare. For masses $M > 4 \times 10^{14}\, h^{-1}\, M_\odot$, we find excellent agreement for the options we prefer on physical grounds, homogeneous ellipsoid dynamics and binary exclusion. This corresponds to peaks with density height relative to the rms of $\nu_{\rm pk} \gtrsim 1.7$. We show we are somewhat resolution limited in a 200 h^{-1} Mpc box in the peaks method for lower masses to allow accurate determination of the distributions. Direct spatial comparisons between the P^{3}M groups and the corresponding peaks also show good agreement (§ 3.3). All P^{3}M groups with more than 400 particles ($M_{\rm gp} \geq 4.2 \times 10^{14}\, h^{-1}\, M_\odot$) can be matched to peaks that are quite nearby, and the masses and internal energies are well correlated. Further, we find the matched peaks and groups obey nearly the same relationship between mass and internal binding energy.

2.1. *Group Finding Based on Average Interior Density*

The most popular cluster-finding method is the percolation or "friends-of-friends" algorithm. Particles are joined together in a group if they belong to a percolation chain, overlapping with at least one neighbor at most a distance $p\bar{n}^{-1/3}$ away. Here $\bar{n}$ is the average particle density within the simulation volume and p is the percolation parameter. Percolation group finding can be viewed in a different way which is better suited to us. The overdensity field,

$$1 + \delta(\boldsymbol{x}, t) \equiv \rho(\boldsymbol{x}, t)/\bar{\rho}\,, \tag{2.1}$$

is smoothed with a "top hat" filter of radius $p\bar{n}^{-1/3}$ and the groups are identified with connected volumes of space lying above the threshold,

$$1 + \delta_{S\rm cut} = \frac{3}{2\pi p^3}; \qquad \text{i.e., } n/\bar{n} \geq 2\,. \tag{2.2}$$

This assumes that the mass per particle m_0 is constant, and $\bar{\rho} = m_0\bar{n}$. Thus the percolation method tries to define an outer contour of density as the grouping criterion (hence S for surface). With a percolation parameter $p = 0.2$, we have $1 + \delta_{S\rm cut} = 60$. Our hierarchical peaks method was designed to mimic a cut, $\delta_{V\rm cut}$, at a specific volume-averaged overdensity $\langle\delta\rangle_V$, not an outer density contour. If the density profile within a cluster has a spherical power-law form, $\delta(r) \propto r^{-\gamma}$, then we would have

$$\delta_{V\rm cut} = \frac{3}{3-\gamma}\,\delta_{S\rm cut}\,. \tag{2.3}$$

For $\gamma = 2$, this gives $\delta_{V\rm cut} \approx 176$, which is why $p = 0.2$ has been a common choice among N-body simulators, since $\delta = 179$ is what a spherical top hat collapse would give for the virialized volume-averaged overdensity. Choosing $p = 0.3$ gives $\delta_{S\rm cut} = 18$ and $\delta_{V\rm cut} \approx 54$. However, the contour interiors are often not spherical and the sphericalized profile may not have $\gamma = 2$. In particular, percolation groups cut at the same threshold may be quite different dynamical entities, with some being long and stringy and some being compact.

Our goal is to identify virialized objects, since these are what our peak patches purport to find. To virialize, a number of orbital crossing times across the group are required. For a spherical region, the crossing time $\propto (1 + \langle\delta\rangle_V)^{-1/2}$. Thus, although volume-

averaged overdensity is not a perfect indicator of crossing time for nonspherical shapes, it is much better than outer contour level. We therefore developed a new efficient group finding method that does select on $\langle\delta\rangle_V$.

In any group finder, there are three basic ingredients: finding a starting particle or location, choosing the next candidate particle to add to the group, and stopping the group building once some criterion such as a density cut is met. Before describing ours, we review how these steps are taken in the minimal spanning tree implementation of the friends-of-friends algorithm (e.g., Carlberg & Couchman 1989). The minimal spanning tree uniquely links the particles together based on neighbor distances. One identifies the groups by severing the links at a maximum allowed link length, $l_{\rm max} = p\bar{n}^{-1/3}$. In this case, the starting particle for a group is any particle not already in a group. The next particle as a candidate for group membership is any one that is linked to a particle already in the group. It is accepted if the link length is below $l_{\rm max}$. The stopping criterion is that all links to the group have been checked. Groups found with this method are clearly percolated patches of particles, with outer number density contour $n \sim l_{\rm max}^{-3}$.

We have developed a group finder that calculates a "smooth-particle overdensity" (SPO) for a cluster of particles. The algorithm is presented in Appendix A. The SPH-style smoothing kernel is used to interpolate smoothed field quantities—such as density, velocity, and temperature (velocity dispersion)—onto the particles. Particles having a high smoothed density ρ_p are tagged as cluster "seeds," and a group is grown radially around the seed until a volume-averaged overdensity $1 + \langle\delta\rangle_V = (M_{\rm gp}/V_{\rm gp})/\bar{\rho}_{\rm nr}$, relative to the cosmological background density $\bar{\rho}_{\rm nr}$, reaches the critical value $\delta_{V{\rm cut}}$. Because the group is grown radially from a center, all the group-member particles are contained within some sphere, although of course the particles will have in general some nonspherical distribution. The SPO group-finder is akin in philosophy to the peak-patch picture of averaged fields within spherical Lagrangian volumes; in some sense this is the discretized analog.

A summary of the numbers of groups found using the overdensity method for different $\delta_{V{\rm cut}}$ and percolation method for different p is given in Table 1. In Figure 1, we compare the mass function determined with our group-finder with that determined with the percolation method. The mass function is defined to be the average density in objects above mass M (in units of the critical density $\rho_{\rm cr}$),

$$\Omega(>M) \equiv \frac{1}{\rho_{\rm cr} V_{\rm box}} \int_M^\infty m d\ln m \frac{dn_{\rm gp}}{d\ln m} = \frac{1}{\rho_{\rm cr} V_{\rm box}} \sum_{M_g > M} M_g , \tag{2.4}$$

where $V_{\rm box}$ is the simulation volume ($200^3\ h^{-3}$ Mpc^3). We show results for overdensity cuts $\delta_{V{\rm cut}} = 180$ and $\delta_{V{\rm cut}} = 100$. The value of 180 is the fiducial one we use throughout this paper, since it is the virial equilibrium overdensity that a spherical top-hat collapse model gives (for a $\Omega = \Omega_{\rm nr} = 1$ universe like the CDM model used here). For the percolation method, we show results for $p = 0.2$ and $p = 0.3$, for which group membership is determined from Carlberg & Couchman's minimal spanning tree. These results show that the $p = 0.2$ mass function is reasonably close to the $\delta_{V{\rm cut}} = 180$ one, as one expects based upon the argument for spherical isothermal halos with $\gamma \approx 2$ given above. A combination of slightly steeper profiles than $\gamma \approx 2$ and slightly fuzzier distributions for the smooth-particle overdensity groups seem to explain why it is a little less. That the two methods do not give exactly the same group membership is illustrated in Figure 2, where a projection onto the $x - y$ plane of the inner $(150\ h^{-1}\ {\rm Mpc})^3$ volume of the $(200\ h^{-1}\ {\rm Mpc})^3$ cube shows that percolation groups are not as rounded as those cut using the mean interior density and there are $\delta_{V{\rm cut}} = 180$ groups that do not appear among the $p = 0.2$ groups, while all $\delta_{V{\rm cut}} = 180$ groups appear in the $p = 0.3$ catalog.

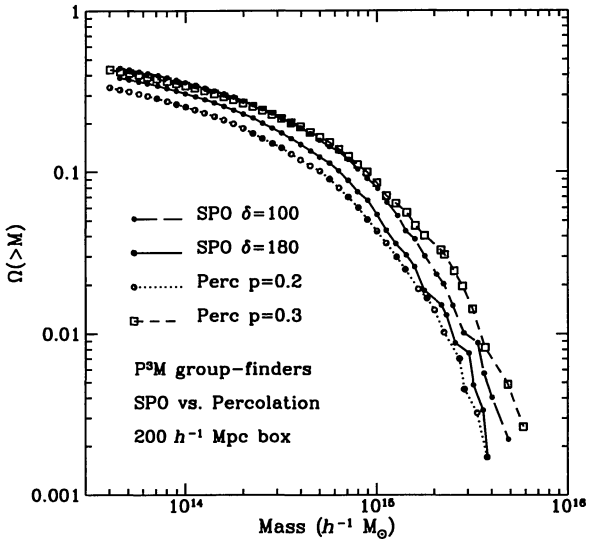

FIG. 1.—The mass functions of the Couchman P^{3}M groups in the 200 h^{-1} Mpc box for different group-finding algorithms: our "smoothed-particle overdensity" method which truncates group membership once a threshold volume-averaged interior overdensity is reached (*filled circles*, for $\delta_{V{\rm cut}} = 180$ and $\delta_{V{\rm cut}} = 100$); the percolation friends-of-friends method using link lengths of $p = 0.2$ (*open circles*) and $p = 0.3$ (*open squares*).

TABLE 1

VARYING THE GROUP-FINDER FOR THE P^{3}M SIMULATION

Group-finder	Cut	n_{400+}[a]	n_{200+}[b]	n_{100+}[c]
Overdensity	$\delta_{Vcut} = 100$	483	1146	2403
Overdensity	$\delta_{Vcut} = 180$	381	1005	2157
Overdensity	$\delta_{Vcut} = 500$	244	698	1710
Percolation	$p = 0.3$	457	1049	2173
Percolation	$p = 0.2$	308	807	1822

[a] Groups with 400 or more particles; $M_{gp} \geq 4.212 \times 10^{14} h^{-1} M_\odot$.
[b] Groups with 200 or more particles; $M_{gp} \geq 2.106 \times 10^{14} h^{-1} M_\odot$.
[c] Groups with 100 or more particles; $M_{gp} \geq 1.053 \times 10^{14} h^{-1} M_\odot$.

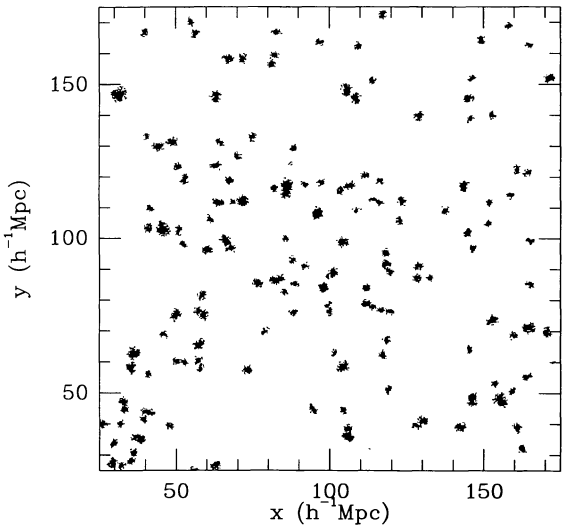

FIG. 2*a*

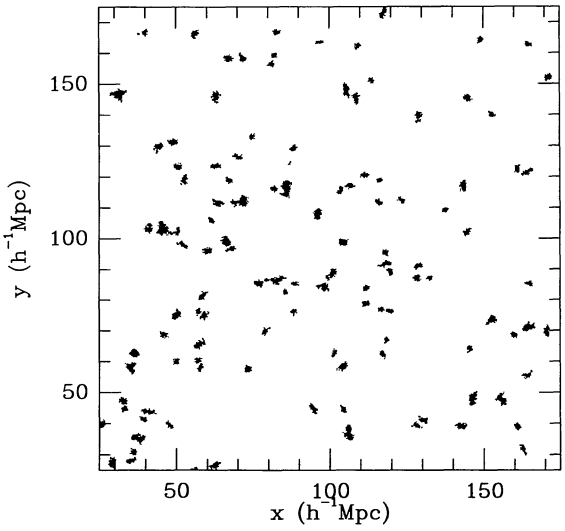

FIG. 2*b*

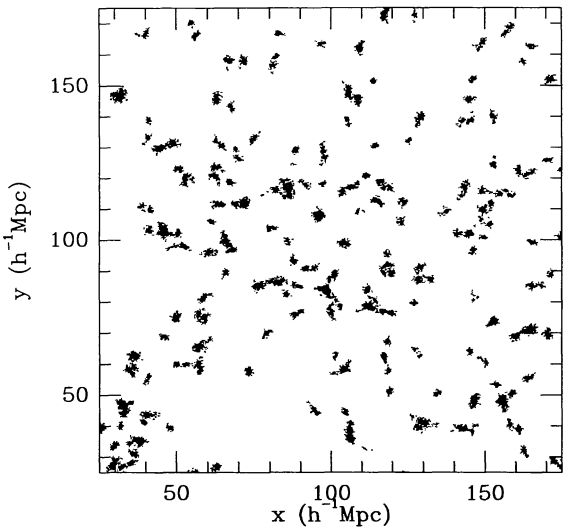

FIG. 2*c*

FIG. 2.—A comparison of the projected (x, y) particle content of our $\delta_{Vcut} = 180$ groups (*a*) with that of $p = 0.2$ percolation groups (*b*) and $p = 0.3$ percolation groups (*c*), for the inner (25–175) h^{-1} Mpc region of the 200 h^{-1} Mpc box. The groups in this plot have more than 400 particles, $M_g > 4.21 \times 10^{14} h^{-1} M_\odot$. Note that some of our groups are not among the $p = 0.2$ groups and the particle distributions differ at the outer edges.

2.2. *Interior Group Energies and Virialization*

We also compute the kinetic, potential, and internal energies of the groups. To put the comparison of these energies on the same footing, we express them in terms of three-dimensional velocities:

$$v_K^2 \equiv 2\frac{K}{M_g}, \qquad K \equiv \frac{1}{2}\sum_{p=1}^{n_g} m_p |\boldsymbol{v}_p - \boldsymbol{v}_g|^2,$$

$$v_W^2 \equiv -\frac{W_{\rm int}}{M_g}, \qquad W_{\rm int} \equiv -\frac{1}{2}\sum_{p=1}^{n_g}\sum_{q\neq p}^{n_g} \frac{Gm_p m_q}{\bar{a}(|\boldsymbol{x}_p - \boldsymbol{x}_g|^2 + \epsilon^2 h^2)^{1/2}}, \tag{2.5}$$

$$v_E^2 \equiv -2\frac{E_{\rm int}}{M_g} = -v_K^2 + 2v_W^2, \qquad E_{\rm int} \equiv K + W_{\rm int}.$$

Thus v_K is the group velocity dispersion. In the expression for the internal gravitational potential $W_{\rm int}$, we include a softening ϵh to avoid divergences; here, $h = h_p$ is the smoothing scale for the central particle in the group, and we take $\epsilon = 0.03$, which results in a smaller softening than that actually used by Couchman for his P^{3}M run.

In isolated virial equilibrium, all three velocities would be equal. The general case has correction terms which cannot be determined very well from P^{3}M output at a single simulation time step. Let us consider the terms that can modify the equality in the case in which the group interior has a spherical boundary. The trace of the tensor virial theorem (e.g., Binney & Tremaine 1987) can be written in terms of an asymmetry Δ_E in the isolated virial velocity relations:

$$v_E^2 = v_K^2 - 2\Delta_E^2, \tag{2.6a}$$

$$v_W^2 = v_K^2 - \Delta_E^2, \tag{2.6b}$$

$$\Delta_E^2 = 3\frac{P_{{\rm rr},S}}{\langle\rho\rangle_V} - \frac{W_{\rm int-ext}}{M_g} + \frac{1}{2}\frac{d^2}{dt^2}\,{\rm Trace}\,(Q). \tag{2.6c}$$

Here, $P_{{\rm rr},S}$ is a radial surface pressure, Trace (Q) is the trace of the moment of inertia (or mass quadrupole) tensor Q_{ij} and $W_{\rm int-ext}$ is the interaction potential energy between the interior of the group and the exterior (more precisely, the contribution to the virial of the interior from the gravitational field of exterior particles). External gravitational forces can help or hinder the binding of the interior particles depending upon how they are arrayed compared with sublumps in the group. The surface pressure correction in a dark matter distribution arises if we think of the medium as continuous and described by a one-particle distribution function, rather than in terms of discrete particles. It arises because there may be an asymmetry at a "microscopic" level between particles whose orbits take them outward through the boundary and those coming in. This term will invariably lower the v_E relative to v_K. Consider the case of a group that has had a recent merger, a very common possibility in hierarchical scenarios. The particles get overcompressed relative to the virial equilibrium, overshoot, then have damped oscillations as they settle into a true isolated equilibrium. The changing spherical moment of inertia "stores" some of this energy mismatch.

We also calculate the "circular velocity":

$$v_{\rm circ}^2 = GM_g/R_g, \tag{2.7}$$

which is one of the conventional ways of characterizing the potential well depth of a group. For a spherical $\delta(r) \propto r^{-\gamma}$ profile, well beyond the core radius, we have $v_{\rm circ}^2 \approx [(5-2\gamma)/(3-\gamma)]v_W^2$. For the $\gamma = 2$ isothermal halo, we have $v_{\rm circ}^2 \approx v_W^2$. We shall show that the circular velocity does in fact come close to v_W for the Couchman groups.

Which P^{3}M group energy should we use to compare our peak internal energy to? Clearly it is v_E^2 that $v_{E,{\rm pk}}^2$ is designed to measure. On the other hand, when we wish to predict observables for group catalogs, it may be v_K^2 which is more appropriate. (See BM3 for a discussion.)

We show in Figure 3 how close the P^{3}M clusters found using our group-finder are to isolated virial equilibrium (i.e., $\Delta_E = 0$). The three panels show three choices for the mean interior density threshold, $\delta_{V{\rm cut}} = 100$, 180, and 500 for (a), (b), and (c), respectively. A measure of the substantial average departure from equilibrium is $v_W/v_K \sim 0.92$, which translates to a 15% deviation of $|W_{\rm int}|/(2K)$ from unity. The overdensity cut does not affect this very much. If we use Couchman's softening of the gravitational force, which is the correct one to use to determine whether virial equilibrium prevails, the v_W/v_K discrepancy will be only slightly larger.

3. EVALUATION OF THE HIERARCHICAL PEAK-PATCH ALGORITHM

In the following two subsections, we compare the hierarchical peaks method with the P^{3}M simulation using volume averaged one-point distribution functions for the mass and velocity dispersion. In the subsequent two subsections, we directly compare the

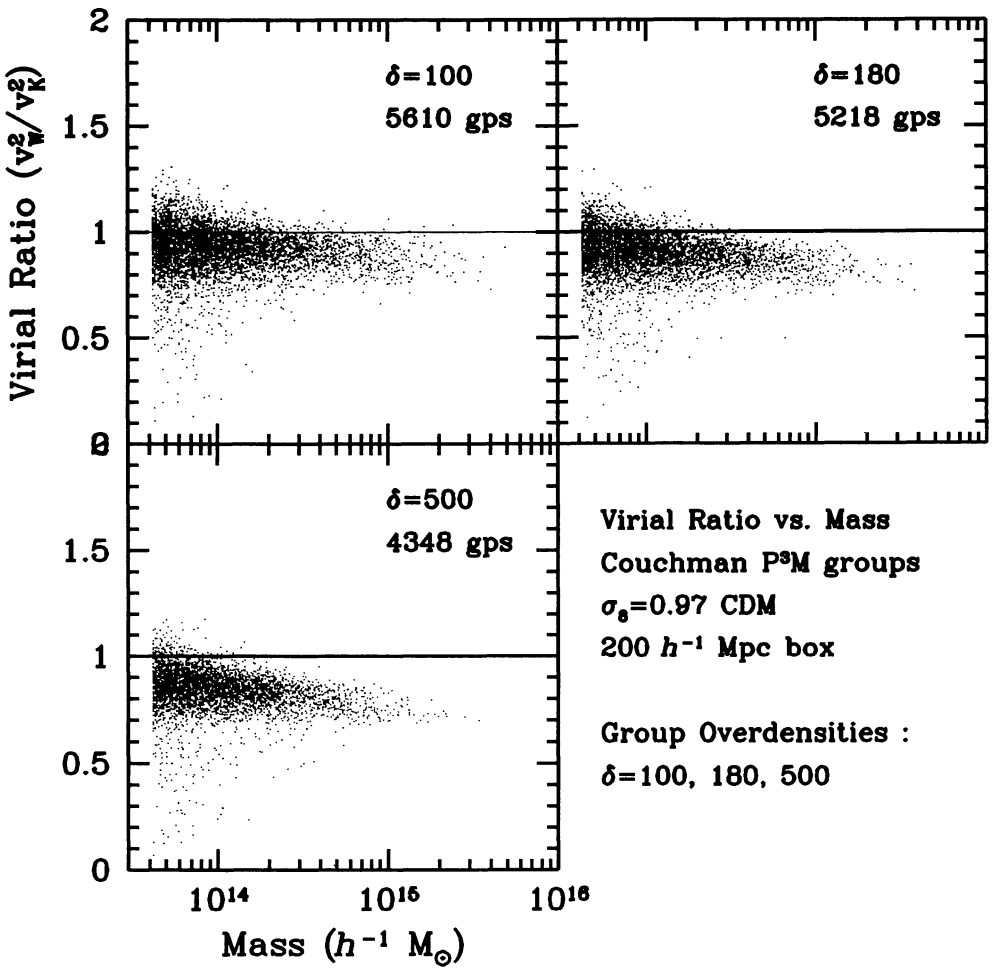

FIG. 3.—The virial ratios ($v_W^2/v_K^2 \equiv -W_{\rm int}/2K$) for the Couchman P^{3}M groups found using the smoothed particle overdensity algorithm. The three panels show the ratios versus group mass for the three overdensities $\delta_{V\rm cut}$ = 100, 180, and 500. In isolated virial equilibrium this ratio is unity, hence equilibrium is not the norm. Note that there is little difference between the three overdensities, except for a slight trend of decreasing ratio with increasing overdensity.

peak patches and the P^{3}M groups. For the P^{3}M data, we use the groups found with our overdensity algorithm described above, with an overdensity cut $\delta_{V\rm cut}$ = 180 (because it is the virial equilibrium overdensity that a spherical top-hat collapse model gives). The hierarchical peaks are implemented as described in BM1, using a hierarchy of 25 Gaussian filters, spaced logarithmically from $R_G = 2.0\ h^{-1}$ Mpc to $R_G = 8.0\ h^{-1}$ Mpc. The relationship between enclosed mass and Lagrangian spherical top-hat radius is

$$M_{\rm TH} = \frac{4\pi}{3}\bar{\rho}_{\rm nr}R_{\rm TH}^3 = 1.156\times 10^{12}(R_{\rm TH}/h^{-1}\ {\rm Mpc})^3\, h^{-1}\, M_\odot\,. \tag{3.1}$$

The lattice size was $a_{\rm L} = 1.5625\ h^{-1}$ Mpc, and the corresponding P^{3}M particle mass was $M_p = 1.053\times 10^{12}\ h^{-1}\ M_\odot$.

3.1. *The Mass Function*

The mass function is defined by equation (2.4). In Figure 4, we show how the mass functions $\Omega(>M)$ for the peaks found using the ellipsoidal and spherical approximations to internal dynamics fare with respect to the mass function of the P^{3}M groups. Binary reduction was used to deal with Lagrangian overlaps for the peaks. The mass function for the ellipsoidal peaks agrees quite well with that for the N-body groups for masses $M > 3\times 10^{14}\ h^{-1}\ M_\odot$; below that, the peaks' function falls below the P^{3}M function. The peaks mass function with spherical dynamics is offset upward in mass by $\sim$20% at the high-mass end. The average offset for masses above $4\times 10^{14}\ h^{-1}\ M_\odot$ is 23%. Note that this is only a 7% correction in $R_{\rm pk}$, which is the quantity we measure; at $4\times 10^{14}\ h^{-1}\ M_\odot$ ($R_{\rm pk} = 7.02\ h^{-1}$ Mpc) this corresponds to $\Delta R \approx 0.5\ h^{-1}$ Mpc which is only $0.3a_{\rm L}$. It certainly appears from this one-point function that the N-body data prefers the more physically correct ellipsoidal model over the spherical one.

A useful comparison mass is $M_{\rm TH,*}$ (eq. [3.1]), the mass associated with the top-hat filter scale $T_{\rm TH,*}$ at which the linear rms

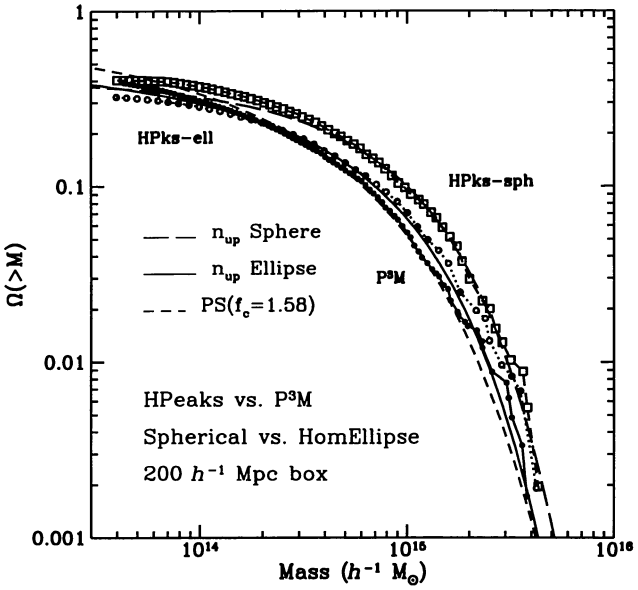

FIG. 4.—The mass function (fraction of the closure density found in objects above a given mass M) for peak-patches compared with that for P^{3}M groups, for the $\sigma_8 = 0.97$ CDM model. The N-body clusters have 40 or more particles ($M_g > 4.21 \times 10^{13}\ h^{-1}\ M_\odot$) and a volume-averaged density contrast above $\delta_{Vcut} = 180$. Analytic functions for peaks that just pierce the density threshold f_c for spherical dynamics (*long-dashed curve*, $f_c = 1.686$) and for ellipsoidal dynamics [solid, $f_c(e_v)$], and for the Press-Schechter formula (*short-dashed curve*, $f_c = 1.58$) are shown. The peak mass function with ellipsoidal dynamics and the PS curve matches the P^{3}M group mass function; for spherical peak-dynamics to match, about a 20% mass reduction is needed. (The PS formula with $f_c = 1.686$ is offset to lower masses [BM1].)

density fluctuations are equal to 1.686, i.e., $\sigma_0(R_{TH,*}) = f_c$. The maximum of the differential Press-Schechter mass function occurs at $M_{TH,*}$. This scale corresponds to $\nu = 1$ fluctuations, very far from the rare-event regime. For the $\sigma_8 = 0.97$ CDM model, $M_{TH,*} = 0.9 \times 10^{14}\ h^{-1}\ M_\odot$. We draw attention to Figure 12 of BM1, which compares the PS mass function with that for hierarchical peaks. We also show the PS curve with density threshold $f_c = 1.58$, which fits the data on the "rare-event" side. (For the standard value $f_c = 1.686$, the curve is too low.) The good agreement between the Press-Schechter mass function and that for N-body groups around $M_{TH,*}$ was shown by Bond et al. (1991) for a set of rather small power-law N-body simulations, but we have now extended this comparison to the extreme Gaussian tail of the mass function and shown that only small modifications are necessary to justify continued application of the easy-to-use Press-Schechter formula.

Superposed on the Monte Carlo points are analytic curves using only the peak points which are just piercing upward through the linear density threshold f_c (upcrossing peaks). Two curves are shown. The higher one has no extra exclusion beyond the (powerful) one associated with the restriction to those peaks with $F = f_c$. The second is an attempt to approximate the half-exclusion case. At least for object counting, half-exclusion and binary exclusion are the same. Formulae for the curves are given in Bond (1989) and, with a more refined mass estimator and f_c, in BM4. The analytic curves were derived using the same CDM power spectrum normalized to $\sigma_8 = 0.97$ as in the simulations, but of course the result shown is an ensemble-average rather than a volume average over the box. The analytic peak functions are in excellent agreement with the Monte Carlo peak points for both the spherical approximation to dynamics which has a constant $f_c = 1.686$ and for homogeneous ellipsoid dynamics, for which $f_c(e_v)$ is a function of the mean ellipticity e_v, and, through this, a function of mass. An approximate expression for $f_c(e_v)$ is given in BM4.

The ellipsoidal collapse model significantly improves agreement with the N-body data relative to that with the spherical top-hat collapse model. We emphasize that we were led to the extra complication of ellipsoidal dynamics because we felt it was essential on physical grounds to include the influence of shear upon the internal patch evolution. It was not to tweak the agreement with the N-body data. That was a bonus.

In Figure 5, we compare mass functions with some of the other choices for candidate peak points with that for Gaussian-filtered density peaks with threshold $f_t = 1.686$, our standard method. (The reason we do not directly use top-hat filtering to create the candidate point list was discussed in BM1, § 3.3). We use homogeneous ellipsoid dynamics and binary reduction for our exclusion algorithm in all cases. Out of the 128^3 grid cells in the entire 200 h^{-1} Mpc box, we find a total of 7647 peaks above $f_t = 1.686$; of these peak patches, 7615 successfully collapse using the ellipsoid model. After half-exclusion and binary reduction, we are left with 3530 peaks (on all filter scales). We also consider density peaks with a lowered threshold, $f_t = 0.01$ (nonzero to allow e_v and p_v to be defined). The mass function for these peaks is very similar to that of the standard density peaks and that of the λ_{v1} peaks (described below), so we do not show it in Figure 5. The counts of peaks found in our box, at various stages of the process, are listed for the different peak-finding methods in Table 2. Above a mass cut of $4.21 \times 10^{14}\ h^{-1}\ M_\odot$ (corresponding to 400 or more grid cells or P^{3}M particles), there are only 3.4% more $f_t = 0.01$ final peaks than for those chosen with $f_t = 1.686$; using $f_t = 1.686$ results in a saving of 34% in number of candidate points to consider.

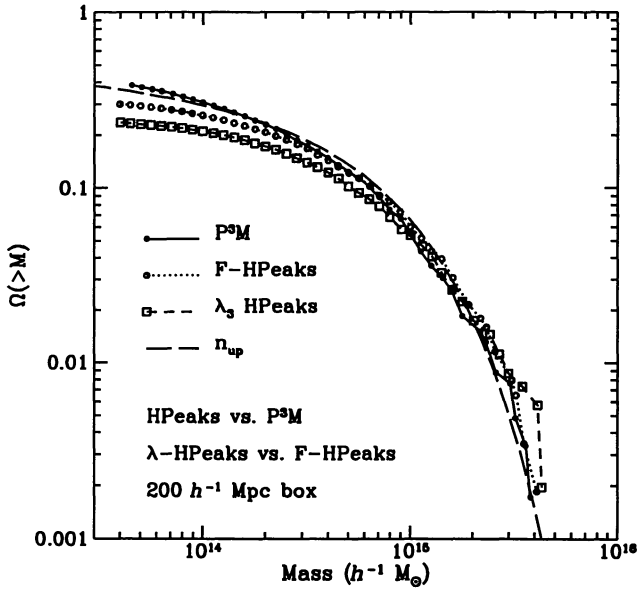

FIG. 5.—Comparison with the *N*-body data (*filled circles, solid line*) of the mass function for *F*-peaks above a threshold $f_t = 1.686$ (*open circles, dotted line*) and for λ_{v3} peaks above a threshold $f_t = 0.01$ (*open squares, dashed line*). Both used ellipsoidal dynamics and binary reduction. The analytic upcrossing formula with ellipsoidal dynamics is the long-dashed curve. The density peak mass function fits the P^{3}M function best. The λ_{v1}-peak and *F*-peak functions with $f_t = 0.01$ are quite similar to the $f_t = 1.686$ *F*-peak shown (BM1).

In BM1, we introduce the strain eigenvalues $\lambda_{v3} \geq \lambda_{v2} \geq \lambda_{v1}$, which we parameterized in terms of $F = \lambda_{v3} + \lambda_{v2} + \lambda_{v1}$, and the shear ellipticity e_v and prolacticity p_v. Since the pancake picture of structure formation has the first objects forming at peaks of λ_{v3}, it is natural to see what difference it makes if we use those points as candidate points. The Zeldovich approximation to dynamics shows that initially the flow in comoving space is convergent upon a point if $\lambda_{v1} > 0$. It may thus seem natural to consider points at which the convergence is maximized. However, the homogeneous ellipsoidal dynamics shows that the nonlinear tidal forces which the Zeldovich approximation neglects can cause patches with $\lambda_{v1} < 0$ to collapse along all three axes. Nonetheless, it is interesting to see what would happen if these points are chosen as candidate points.

Using grid points which are peaks in λ_{v3} which also have the filtered density field *F* in excess of $f_t = 0.01$ (again to allow e_v and p_v to be defined), we obtain the mass function shown in Figure 5. This curve tracks the standard density-peak mass function well throughout most of the mass range, extending a bit to higher masses, and saturating at low masses because there are not as many small-scale filter λ_{v3} peaks. The λ_{v1} peak mass function (not shown in Figure 5, but see BM1 Figure 13, is very close to that for the *F* peaks. From Table 2 we see that there are significantly more candidate λ_{v1}-peaks, although after collapse and exclusion the numbers are more similar, especially when a mass cut is imposed. The reason there are also slightly more λ_{v3}-peaks than *F* peaks with the same $f_t = 0.01$ threshold on *F* is because there will be some uncounted *F* peaks with $F_{pk} < 0$, but since λ_{v3} must exceed $F/3$ always, there will be fewer uncounted $\lambda_{v3} < 0$ peaks.

From Figure 5, we see that our "preferred" choice of $f_t = 1.686$ density peaks is also preferred by the P^{3}M data. A direct peak-to-group comparison using the *N*-body groups (§ 3.4) also shows this. It is also *much* more efficient to compute candidate points based

TABLE 2

VARYING THE CANDIDATE PEAK FINDER IN THE COUCHMAN BOX

Peaks	f_t	n_{pks}[a]	n_{coll}[b]	n_{exc}[c]	n_{400+}[d]	n_{200+}[e]	n_{100+}[f]
F peaks	1.686	7647	7615	3530	350	830	1614
F peaks	0.01	11598	10710	4324	362	843	1582
λ_{v3} peaks	0.01	12378	7840	3291	301	680	1262
λ_{v1} peaks	0.01	19784	14406	5267	363	901	1742

[a] All peaks, all filters.
[b] After ellipsoidal collapse.
[c] After half-exclusion and binary reduction.
[d] $M_{pk} \geq 4.212 \times 10^{14} h^{-1} M_\odot$ (400+ cells).
[e] $M_{pk} \geq 2.106 \times 10^{14} h^{-1} M_\odot$ (200+ cells).
[f] $M_{pk} \geq 1.053 \times 10^{14} h^{-1} M_\odot$ (100+ cells).

on F than on λ_{vj}, especially if we can also add a $f_t = 1.686$ threshold to reduce the number; accordingly, we adopt this choice as our standard.

In Figure 6, we explore the effect of the exclusion or mass-reduction method on the mass function. We compare full exclusion and binary reduction results for the Monte Carlo peaks (using ellipsoidal dynamics) to the mass function for the P^{3}M groups. The curve for the full exclusion falls away from the binary-reduced curve for peak masses $M_p < 5 \times 10^{14}\ h^{-1}\ M_\odot$, since smaller peaks on the outskirts of the larger peaks are eliminated by full exclusion but not by binary reduction. We also show the mass function if we take no exclusion into account (except of course we do not count points at the same site more than once). This curve does not correct the cloud-in-cloud problem and so is expected to lie well above the other curves and not agree with the P^{3}M results, and that is indeed the case.

We adopted binary reduction as opposed to full exclusion because we were worried about an overmerging problem. Once again, an improvement in the physics has led to a better match with the N-body data. Although one could make the reduction method more refined still, we feel that binary reduction is a reasonable option for Lagrangian mass allocation and is the one we adopt as standard. Note that the Monte Carlo peak points with binary reduction lies between the two up-crossing analytic curves, one with and one without an approximate half-exclusion correction. Thus, we can also conclude that the analytic mass function will be sufficiently accurate for many applications, when ease of calculation is a priority.

The drop in the peak density relative to the P^{3}M mass function, for $M \lesssim 4 \times 10^{14}\ h^{-1}\ M_\odot$, is most likely due to loss of short-wavelength information on the large grid. We have checked this hypothesis by simulating two boxes from a $\sigma_8 = 0.97$ CDM power spectrum with random initial conditions, one box of size $L = 200\ h^{-1}$ Mpc, and a box of one-half this length, $L = 100\ h^{-1}$ Mpc. The mass functions are shown in Figure 7 and compared with the Couchman P^{3}M function, which had initial conditions derived from the same power spectrum but with now a different realization. We see that the peak mass function in the smaller box now matches that of the P^3M, in the mass range from $M \lesssim 2 \times 10^{15}\ h^{-1}\ M_\odot$ all the way down to the 40 particle limit of the simulation $M_g = 4.21 \times 10^{13}\ h^{-1}\ M_\odot$, below which the group finding becomes prohibitively unreliable. In the $200\ h^{-1}$ Mpc box, the lattice size is $a_L = 1.56\ h^{-1}$ Mpc, and the Lagrangian top-hat radius corresponding to the divergent mass is $7\ h^{-1}$ Mpc. Note that the Monte Carlo peaks mass function as extended by the smaller box now follows the analytic peak curve for upcrossings without statistical exclusion. Since the P^{3}M calculation in the $200\ h^{-1}$ Mpc box began with the same initial conditions as our calculation, it might be argued that adding a factor of 2 higher frequency waves is incorrect. There are two reasons why we believe this is reasonable for comparing with the Couchman simulation: first, we use a Gaussian filter with $R_G = 0.5 a_L$ on the initial density field when we determine candidate point survival (as a collapsed object) and compute masses. Second, the P^{3}M calculation has an unavoidable noise associated with particle discreteness (shot noise) that can begin the clustering process, which will affect the small mass object count. We (fortunately) have no such spurious effect. Notice that, as expected, the mass function of the $100\ h^{-1}$ Mpc box does not extend to as large a mass as that for the $200\ h^{-1}$ Mpc box. To remedy this, we would add a long-wavelength component, as described in BM1, § 4, and BM1, Appendix D.

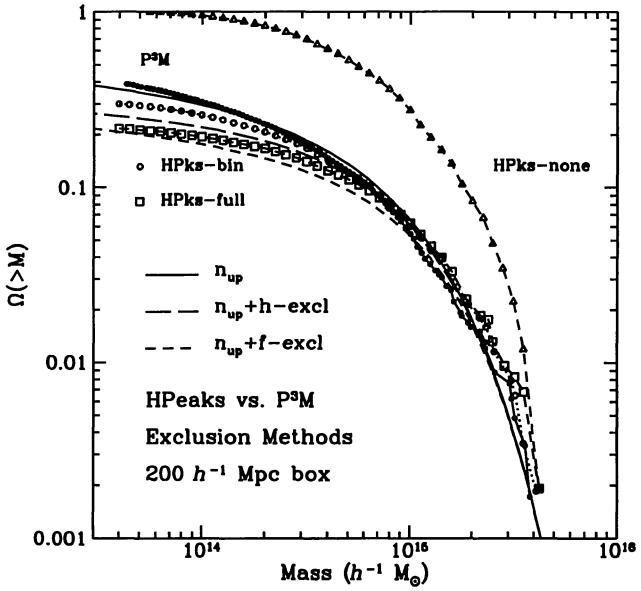

FIG. 6.—The mass functions for F peaks with full exclusion (*large squares*), binary reduction (*small open circles*), and for no Lagrangian exclusion (*small triangles*) are compared with that for the P^{3}M groups (*small filled circles*). The analytic curve for number of "upcrossings" peaks, n_{up}, just piercing the critical density contour $F_{pk} = f_c$ is the solid curve, and the long-dashed and short-dashed curves add a further reduction designed to approximate half-exclusion and full exclusion, respectively. The candidate threshold $f_t = 1.686$ and ellipsoidal dynamics were adopted for the F peaks. The no-exclusion case (except no pixel redundancy is allowed) grossly overcounts overlapping peaks. The full exclusion and binary reduction methods differ at low masses since smaller peaks on the periphery of larger ones are destroyed in the full exclusion operation.

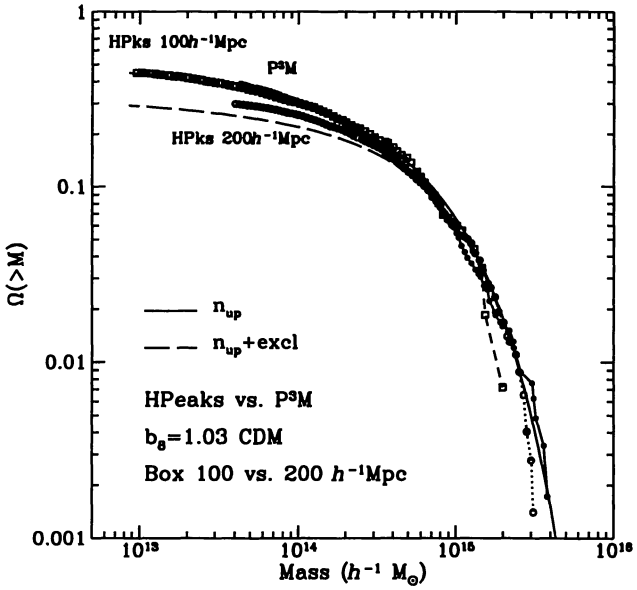

FIG. 7.—The mass functions for Monte Carlo hierarchical peaks in two boxes, with random initial conditions drawn from a $\sigma_8 = 0.97$ CDM power spectrum, vs. the Couchman P^{3}M simulation. The two peak simulations were realized in a boxes of size $L = 200\ h^{-1}$ Mpc (*open circles*) and $L = 100\ h^{-1}$ Mpc (*open squares*). The peak mass function in the smaller box now matches that of the P^{3}M in the mass range where the larger box results diverge, all the way down to the 40 particle limit of the simulation, $M_g = 4.21 \times 10^{13}\ h^{-1}\ M_\odot$. Also shown are the analytic peaks curves. Note that the upcrossing formula follows the smaller box's small mass rise and the larger box's high-mass tail.

3.2. *Velocity Dispersion Function and Energy-Mass Relations*

We show the number density of objects as a function of the "velocities" associated with group kinetic energies (v_K) and internal energies for the groups (v_E) and peak patches ($v_{E,\rm pk}$) in Figure 8. These show that $v_{E,\rm pk}$ falls between the P^{3}M group internal energy and the dark matter velocity dispersion v_K of the groups: as we will see in the next subsection, the $v_{E,\rm pk}$ are on average 4.3% higher than the group internal $v_{E,\rm gp}$, and 12.8% lower than the group kinetic $v_{K,\rm gp}$. Although $E_{\rm int}$ for the groups is the closest analog to $E_{\rm int,pk}$, we noted in BM1, § 2.1.4, and BM1, Appendix B, that even in the homogeneous ellipsoid model there are tidal heating and cooling effects which cause the internal energy to change as collapse proceeds. We showed that the correction in quadratic order was to add heat to the region, thereby raising the (negative) internal energy, and hence lowering v_E^2, which is just the trend we see. In the spherical approximation to dynamics, one would get no difference.

Note that the internal energy curve for peaks found with ellipsoidal dynamics is the same as that for spherical dynamics. This may appear puzzling because the mass functions differ by ~20%. However, it is simple to understand by considering the linear density profiles around the peaks. Let us recall from BM1, equations (2.27a)–(2.27b):

$$v_{E,\rm pk}^2 \equiv [H(z_{\rm pk})\bar{a}_{\rm pk}R_{\rm pk}]^2 F_{\rm pk} S_{\rm pk}, \qquad S_{\rm pk} \equiv (F_{\rm pk}R_{\rm pk}^5)^{-1}\int_0^{R_{\rm pk}^5} \bar{F}(<R_{\rm TH})\,dR_{\rm TH}^5\,, \tag{3.2}$$

where $\bar{a}_{\rm pk} = (1 + z_{\rm pk})^{-1}$ is the expansion factor when the peak collapses, $R_{\rm pk}$ is the peak radius and $F_{\rm pk} = \bar{F}(<R_{\rm pk})$ is the volume-averaged overdensity within $R_{\rm pk}$. Consider a spherically averaged profile with a power law falloff, $F(r) \propto F_c(r_c/r)^\gamma$, where F_c is the central density, r_c is a "core radius," and we assume r is far beyond r_c. With this form, we have

$$F_{\rm pk} = \frac{3}{(3-\gamma)} F_c(r_c/R_{\rm pk})^\gamma, \qquad S_{\rm pk} = \frac{5}{(5-\gamma)}, \tag{3.3}$$

$$v_{E,\rm pk}^2 = \frac{15}{(3-\gamma)(5-\gamma)}[H(z_{\rm pk})\bar{a}_{\rm pk}r_c]^2 F_c(R_{\rm pk}/r_c)^{2-\gamma}$$

This is $R_{\rm pk}$-independent for $\gamma = 2$. Now, for a density power spectrum with local power-law index $n_s[P_F(k) \propto k^{n_s}]$, we have $\gamma = 3 + n_s$. Thus $n_s = -1$ should give about the same internal energies whether ellipsoidal or spherical dynamics is used, even though there is about a 7% discrepancy in their radii. Of course, this is about the local index for the standard CDM model in the cluster regime. (In the analytic theory, we find that for this CDM spectrum $S_{\rm pk}$ ranges from 1.29 to 1.45 over the relevant filter range.)

For the Press-Schechter case, to form a velocity function most people adopt a phenomenological velocity-mass relation. We show in Figure 8 what form that relation would take in order to fit reasonably well the P^{3}M internal and kinetic energy curves. If we apply

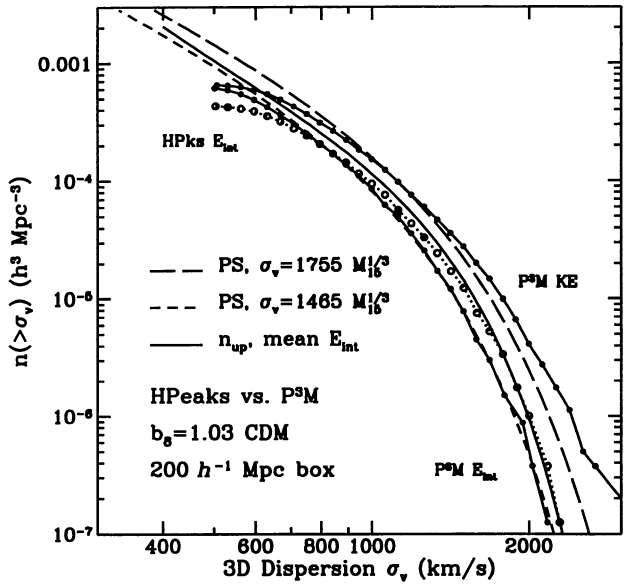

FIG. 8.—The number density of objects with three-dimensional velocity dispersion above σ_v, with σ_v given by v_K, the velocity dispersion determined from the group's internal kinetic energy (*filled circles;* "KE") and by v_E, estimated from the group's internal total energy (*filled circles;* "BE"). These are contrasted with the Monte Carlo estimation $v_{E,pk}$ calculated from the peak patch's internal (binding) energy (*open circles*). The analytic result (*solid curve*) for $f_c(e_v)$ barrier-penetrating peak-patch points, using the mean-field calculation of the internal energy and ellipsoidal dynamics, agrees very well with the Monte Carlo curve. We also show how the Press-Schechter (PS) function fares when we use the phenomenological relation of mass to internal group energy and group kinetic energy that we have found ($M_{15} = M/10^{15}\,h^{-1}\,M_\odot$). The peak curve lies on average 5% in v_E above the group internal energy curve and ~12% in v_K below the kinetic energy curve.

the spherical dynamics model to determine the $E_{int} - M$ relation, and assuming an isothermal ($\gamma = 2$) profile so $S_{pk} \approx \frac{5}{3}$, we get an internal energy law $v_{E,PS} \approx 1540(M_{PS}/10^{15}\,h^{-1}\,M_\odot)^{1/3}$ km s^{-1}. (Using the smaller values that the peaks give for S_{pk} gives a value closer to the internal energy we get for groups below.) The phenomenological law most often used is based upon the temperature in the low-resolution smooth particle hydrodynamics calculations of Evrard (1990), which we also discussed in BM1 § 4.2.2, $v_T \approx 1730(M/10^{15}\,h^{-1}\,M_\odot)^{1/3}$ km s^{-1}. If one uses the temperature to v_K^2 ratio actually measured in the Evrard simulations (e.g., Frenk et al. 1990), one gets $v_K \sim 1900\,(M/10^{15}\,h^{-1}\,M_\odot)^{1/3}$ km s^{-1}. The higher and lower PS curves plotted in Figure 8 have coefficients in the $v - M^{1/3}$ relationship determined by our measured kinetic and internal energy relations (1755 and 1465 km s^{-1}, respectively). The P^{3}M data is fitted very well by the Press-Schechter form for $v_{E,gp}$ and reasonably well for $v_{K,gp}$ (with a deviation at the high velocity-dispersion end).

We now discuss the direct determination of the relationship between the various velocities and the mass of the groups. BM1 Figure 11 depicted $v_{E,pk}$ versus mass for the same initial conditions as for the P^{3}M simulation we are focusing on here. We found that $v_{E,pk} \approx 1560\,(M_{pk}/10^{15}\,h^{-1}\,M_\odot)^{1/3}$ km s^{-1} fits the data reasonably well, although a flatter power of mass (0.29) is preferred. The dispersion about the mean was ~5%. We may also recall from BM1 that the analytic counterpart to the hierarchical peaks theory for ellipsoidal dynamics gives $v_{E,pk} = 1530\,(M_{pk}/10^{15}\,h^{-1}\,M_\odot)^{0.29}$ km s^{-1}, which also accurately fits the mean of the Monte Carlo results.

In Figure 9*a*, the velocity dispersion of the groups $v_{K,gp}$ (i.e., the "kinetic energy velocity") is plotted versus mass M_{gp} for the Couchman P^{3}M groups. The relation follows the power-law $M^{1/3}$ expected phenomenologically for virialized clusters. To test this, we calculate the mean relation versus $M_{15} \equiv M/10^{15}\,h^{-1}\,M_\odot$,

$$\log v_0 = \langle \log (v_{K,gp}/M_{15,gp}^{1/3}) \rangle_{gps}, \qquad \delta = \langle \log (v_{K,gp}/M_{15,gp}^{1/3}) - \log v_0 \rangle_{gps}$$

to find the best fit $v_0\,M_{15}^{1/3}$ law and the deviation δ_v about it. We find

$$v_{K,gp} = 1755 \left(\frac{M_{gp}}{10^{15}\,h^{-1}\,M_\odot} \right)^{1/3} \text{km s}^{-1}, \qquad \delta_v = 6.5\%, \qquad \text{for } M_{gp} \geq 2.5 \times 10^{14}\,h^{-1}\,M_\odot . \tag{3.4}$$

This relation is the solid line in Figure 9*a*. In Figure 9*b*, we show the velocity estimate from the internal gravitational energy $v_{W,gp}$ for the P^{3}M groups versus M_{gp}. For groups $M_{gp} \geq 2.5 \times 10^{14}\,h^{-1}\,M_\odot$ we obtain the best fit

$$v_{W,gp} = 1620 \left(\frac{M_{gp}}{10^{15}\,h^{-1}\,M_\odot} \right)^{1/3} \text{km s}^{-1}, \qquad \delta_v = 5.2\%, \qquad \text{for } M_{gp} \geq 2.5 \times 10^{14}\,h^{-1}\,M_\odot . \tag{3.5}$$

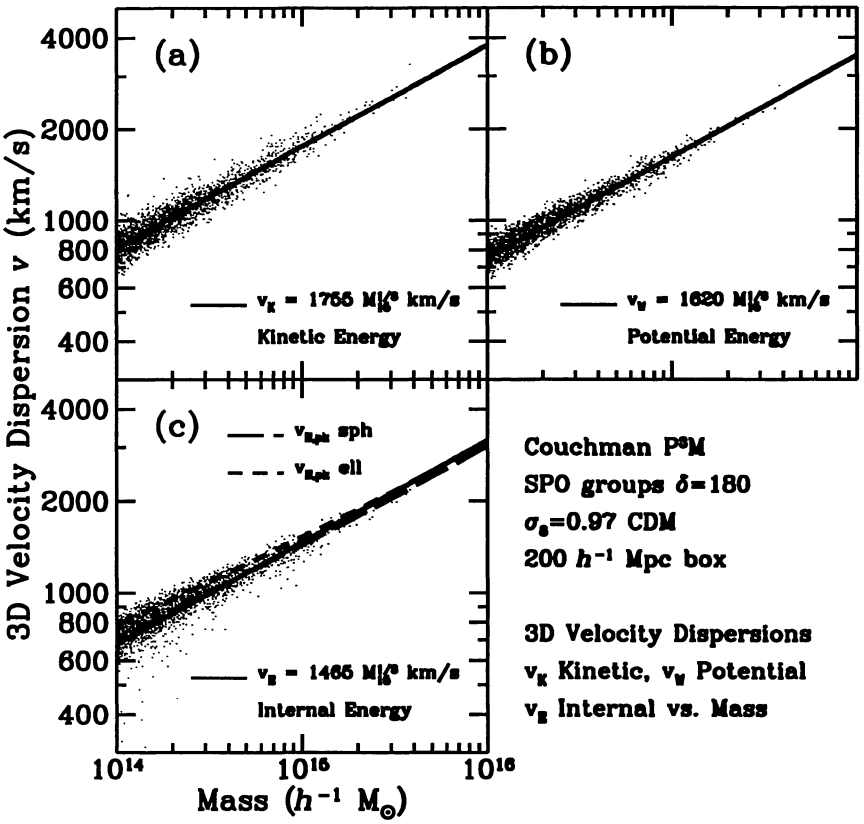

FIG. 9.—(*a*) The three-dimensional velocity dispersion v_K calculated from the Couchman group's kinetic energy is plotted against group mass M_g, along with the best-fit power law $v_K = 1755\,(M/10^{15}\,h^{-1}\,M_\odot)^{1/3}$. (*b*) The velocity $v_W = |W_{\rm int}/M_g|^{1/2}$ estimated from the internal gravitational energy $W_{\rm int}$ of the groups, along with the power-law fit $v_W = 1620\,(M/10^{15}\,h^{-1}\,M_\odot)^{1/3}$. (*c*) $v_E = |2E_{\rm int}/M_g|^{1/2}$ estimated from the internal (binding) energy of the groups, along with a best-fit power-law $v_E = 1464\,(M/10^{15}\,h^{-1}\,M_\odot)^{1/3}$. (A flatter $M^{0.29}$ law is preferred). Analytic curves showing the peak-patch relationships for ellipsoidal (*short-dashed*) and spherical (*long-dashed*) dynamics are in good agreement. (*c*) should be compared with the $v_{E,\rm pk} - M_{\rm pk}$ plot for Monte Carlo peak points shown in BM1.

The circular velocity, equation (2.7), (not shown) has a best-fit $M^{1/3}$ power law given by

$$v_{\rm circ} = 1600\left(\frac{M_{\rm gp}}{10^{15}\,h^{-1}\,M_\odot}\right)^{1/3}\ {\rm km\ s^{-1}}, \qquad \delta_v = 0.2\%, \qquad {\rm for}\ M_{\rm gp} \geq 2.5\times 10^{14}\,h^{-1}\,M_\odot\,. \tag{3.6}$$

The relationship is remarkably scatter free. We have noted that a spherically symmetric isothermal halo profile will lead to $v_{\rm circ} \approx v_W$. This is apparently a reasonable approximation to this P^{3}M data.

In Figure 9*c*, the velocity $v_{E,\rm gp}$ associated with the internal energy is plotted against $M_{\rm gp}$ for the Couchman P^{3}M groups. Our average $M^{1/3}$ power-law fit is

$$v_{E,\rm gp} = 1465\left(\frac{M_{\rm gp}}{10^{15}\,h^{-1}\,M_\odot}\right)^{1/3}\ {\rm km\ s^{-1}}, \qquad \delta_v = 7.8\%, \qquad {\rm for}\ M_{\rm gp} \geq 2.5\times 10^{14}\,h^{-1}\,M_\odot\,. \tag{3.7}$$

There is a somewhat larger dispersion in $v_{E,\rm gp}$ about the $M^{1/3}$ curve than for $v_{K,\rm gp}$. Note that at the lower mass end, there are some marginally bound groups in Figure 9*c*. If we do not fix the $M^{1/3}$ power, the actual $v_{E,\rm gp}$ follows a velocity-mass relation that is somewhat flatter: a least-squares fit gives

$$v_{E,\rm gp} = 1420\left(\frac{M_{\rm gp}}{10^{15}\,h^{-1}\,M_\odot}\right)^{0.29}\ {\rm km\ s^{-1}}, \qquad \delta_v = 7.4\%, \qquad {\rm for}\ M_{\rm gp} \geq 2.5\times 10^{14}\,h^{-1}\,M_\odot\,. \tag{3.8}$$

The rms scatter in $v_{E,\rm gp}$ is only slightly improved over the $M^{1/3}$ fit, but the $M^{0.29}$ law fits the shape better, just as it does for the peaks. The velocities $v_{E,\rm pk}$ for peaks assuming ellipsoidal dynamics are 6.6% higher on average than those for the P^{3}M groups, although the deviation is less for high masses. Curiously, the peak relation assuming spherical dynamics seems to fit rather well. The analytic lines shown in Figure 9*c* demonstrate these points.

For groups, the velocity dispersion, $v_{K,\mathrm{gp}}$, is 19.8% higher than $v_{E,\mathrm{gp}}$, and 12.5% higher than the peaks $v_{E,\mathrm{pk}}$, at the fiducial mass $10^{15}\,h^{-1}\,M_\odot$. However, that is not to say that they do not satisfy the virial theorem when surface pressure, external gravitational field, and moment of interia dynamics are taken into account. In § 2.1, we characterized these extra terms in equation (2.6c) by a mismatch quantity Δ_E with the dimensions of velocity. Using the fits given above, and the $v_E - v_K$ or $v_W - v_K$ virial criterion (eqs. [2.6a]–[2.6b]), we get $\Delta_E^2/v_K^2 \approx 0.15$. This is a measure of the amount by which the P^{3}M groups are out of isolated virial equilibrium in the Couchman simulation.

We note that groups found in the tree and multigrid calculations of constrained fields described in BM1 did have $v_E \approx v_W \approx v_K$ if they were relatively isolated at $z \gtrsim 0.5$ or so. However, in the crowded final cluster state, especially at $z = 0.04$ just after a major merger, the disequilibrium was similar to the magnitude found here, ~7% in v_W/v_K for the multigrid Gauss-Seidel calculation. During and after mergers, the dark matter splashes through the cluster and undergoes a few oscillations before it settles down. Changing the density contour level can capture different aspects of this. At the moment we think the mismatch is a combination of all three effects included in the Δ_E expression. The basic point with the pressure is that there is too much kinetic energy for the internal gravitational attraction within the region, so the particles would expand. This can be compensated by other particles whose orbits take them through the boundary at the same rate as interior particles flow out. If one is interested in the long time evolution of the region, the internal energy may be a better estimator than the instantaneous kinetic energy of the dark matter particles.

3.3. *Direct Comparison of Peak and Group Properties*

We now directly compare the properties of a peak patch associated with a given group with the group's properties. We first need to identify a peak patch with a P^{3}M group. Our approach is to locate the peak closest in position and mass to each group, within some allowed tolerance on differences in position, mass, and/or internal energies of the two. We characterize the level of agreement between the group "gp" and the associated peak "pk" by the following quantities measuring differences in comoving Eulerian position, mass, and velocity dispersions:

$$\delta r_{\mathrm{pk-gp}} = |\boldsymbol{x}_{\mathrm{pk}} - \boldsymbol{x}_{\mathrm{gp}}|, \qquad \delta \log M_{\mathrm{pk-gp}} = \log M_{\mathrm{pk}} - \log M_{\mathrm{gp}},$$

$$\delta \log v_{E,\mathrm{pk-gp}} = \log v_{E,\mathrm{pk}} - \log v_{E,\mathrm{gp}}, \qquad \delta \log v_{K,\mathrm{pk-gp}} = \log v_{E,\mathrm{pk}} - \log v_{K,\mathrm{gp}}.$$

The statistic we use to regulate the matching between the peaks and the groups is

$$\epsilon_{\mathrm{pk-gp}} = \frac{\delta r_{\mathrm{pk-gp}}}{\delta r_0} + \frac{|\delta \log M_{\mathrm{pk-gp}}|}{\delta \log M_0}, \tag{3.9}$$

where δr_0 and $\delta \log M_0$ are normalizing scales for the allowed distance error and log-mass error, respectively. The peak for which $\epsilon_{\mathrm{pk-gp}}$ is a minimum is paired with each group. We limit the matching to peaks less than a maximum distance $\delta r_{\max}$ away and with log-mass errors less than $\delta \log M_{\max}$. Note that a given peak may be associated with more than one group. (We could, conversely, find the groups matched to each peak, in which case there could be more than one group associated with a given peak.)

3.3.1. *Internal Properties*

For groups with $M_{\mathrm{gp}} \geq 2.106 \times 10^{14}\,h^{-1}\,M_\odot$ (i.e., having 200 particles or more for this simulation), we find 1005 total $\delta = 180$ groups in the volume, of which 1003 are bound ($E_{\mathrm{int}}/M < 0$). A summary of the various groups and peaks above a given mass are listed in Tables 1 and 2. There are only 830 peaks above the same mass cutoff, but since the masses may not be the same, we search over a larger mass range, down to the maximum allowed deviation for the search. We take $\delta \log M_{\max} = 0.7$, thus matching peaks within a factor of 5 in mass. We also require that the matching peak be within $\delta r_{\max} = 8\,h^{-1}$ Mpc of the group. This distance is 40% of the mean separation of the 1003 groups above the mass cut, $\bar{n}^{-1/3} = 20.0\,h^{-1}$ Mpc. For the normalization factors, we choose $\delta r_0 = 3\,h^{-1}$ Mpc and $\delta \log M_0 = 0.3$.

We restrict our comparison to the inner $150\,h^{-1}$ Mpc of the box to avoid edge effects. In this volume, we have a total of 435 P^{3}M groups that have 200 or more particles ($M_{\mathrm{gp}} \geq 2.106 \times 10^{14}\,h^{-1}\,M_\odot$), for which we are able to match 431 to 391 distinct peaks (thus some peaks have been associated with more than one group). We compute the mean errors and the standard deviations about the means,

$$\langle \delta r_{\mathrm{pk-gp}} \rangle = 2.0\,h^{-1}\,\mathrm{Mpc} \pm 1.2\,h^{-1}\,\mathrm{Mpc},$$

$$\langle \delta \log M_{\mathrm{pk-gp}} \rangle = -0.021 \pm 0.176 \qquad (-4.7\% \pm 50.0\%),$$

$$\langle \delta \log v_{E,\mathrm{pk-gp}} \rangle = 0.020 \pm 0.047 \qquad (+4.7\% \pm 11.4\%),$$

$$\langle \delta \log v_{K,\mathrm{pk-gp}} \rangle = -0.050 \pm 0.060 \qquad (-10.9\% \pm 12.2\%).$$

Note that the $\sigma[\delta \log M]$ is 3 times that for $\delta \log v_K$, as would be expected for $v_K \propto M^{1/3}$. The $\sigma[\delta \log v_E]$ is lower than $\sigma[\delta \log v_K]$, which suggests a slightly tighter relation for the binding energies.

Different peak selection methods, $f_t = 0.01$ density peaks or λ peaks, lead to somewhat larger errors when compared to the standard $f_t = 1.686$ density peaks. For example, choosing peaks in λ_{v3} results in mean errors of $\langle \delta r_{\rm pk-gp} \rangle = 2.5\ h^{-1}$ Mpc and $\langle \delta \log M_{\rm pk-gp} \rangle = -0.074 \pm 0.230$ ($-15.7\% \pm 69.8\%$), while λ_{v1} peaks give $\langle \delta r_{\rm pk-gp} \rangle = 2.2\ h^{-1}$ Mpc and $\langle \delta \log M_{\rm pk-gp} \rangle = -0.023 \pm 0.186$ ($-5.2\% \pm 53.5\%$). The reduced threshold $f_t = 0.01$ density peaks are nearly as good as the standard $f_t = 1.686$ peaks, with $\langle \delta r_{\rm pk-gp} \rangle = 2.1\ h^{-1}$ Mpc and $\langle \delta \log M_{\rm pk-gp} \rangle = 0.0011 \pm 0.179$ ($+0.25\% \pm 51.0\%$).

In Figure 10, we plot the masses for the paired peaks against those for the groups. For this plot, the groups have mass $M_g \geq 1.053 \times 10^{14}\ h^{-1}\ M_\odot$ (100 or more particles), and the maximum tolerances chosen for pairing peaks were $\delta r_{\rm max} = 5\ h^{-1}$ Mpc and $\delta \log M_{\rm max} = 0.6$. A total of 905 P^{3}M groups were found above this mass cutoff in the inner $150\ h^{-1}$ Mpc region, with a mean separation $\bar{n}^{-1/3} = 15.6\ h^{-1}$ Mpc—the distance limit was lowered to $r_{\rm max} = 0.32\ \bar{n}^{-1/3}$ to damp down spurious associations. Of the 905 groups, 836 were matched with 745 distinct peaks satisfying the criteria. Note that the points lie in a fairly wide distribution about the line of equality, with the core of the distribution following the line more tightly. Of course, some of this may just be because we got the wrong peak for the group in question. After all, Zeldovich dynamics was used to determine the final position for the peaks. As well, some of the upper extension may be due to merging of peaks that are not merged in the group catalog, and vice versa.

In Figure 11 we show the corresponding group and peak velocity dispersions, $v_{E,\rm pk}$ versus $v_{E,\rm gp}$, derived from the internal energy, for the matched peaks and groups above the velocity shown. On average, $v_{E,\rm pk}$ lies 4.8% above the corresponding P^{3}M $v_{E,\rm gp}$, with a dispersion of $\pm 13.5\%$. (The dispersion is slightly higher than for those matched with groups with $M_{\rm gp} \geq 2.106 \times 10^{14}\ h^{-1}\ M_\odot$, as given above.)

3.3.2. *Position and Bulk Velocity Correspondence*

We now investigate the correspondence between the peculiar velocities of the peaks and groups, and the position errors relative to the peak displacements. To the extent that we accept the one-to-one correspondence between the groups and the peaks, for the velocities we can think of this as providing measures of importance of nonlinearities in the flow, since the Zeldovich approximation assumes linear perturbation results for the velocities. As we discussed in BM4, the nonlinear correction should be dependent upon the power spectrum. For the CDM model used here, the nonlinear corrections should be larger than for current popular hybrid models of structure formation, both because the amplitude of the power spectrum on cluster scales is higher here ($\sigma_8 \approx 1$, not $\sigma_8 \approx 0.7$), and because there is not as much relatively long wavelength power, which makes the linear velocities more accurate estimates.

Consider the direction cosines between the peak and group vectors

$$\mu_{V,\rm pk-gp} = \frac{\boldsymbol{V}_{P,\rm pk} \cdot \boldsymbol{V}_{P,\rm gp}}{|\boldsymbol{V}_{P,\rm pk}|\,|\boldsymbol{V}_{P,\rm gp}|}, \qquad \mu_{\delta V,\rm pk-gp} = \frac{(\boldsymbol{V}_{P,\rm pk} - \boldsymbol{V}_{P,\rm gp}) \cdot \boldsymbol{V}_{P,\rm pk}}{|\boldsymbol{V}_{P,\rm pk} - \boldsymbol{V}_{P,\rm gp}|\,|\boldsymbol{V}_{P,\rm pk}|}, \mu_{\delta S,\rm pk-gp} = \frac{(\boldsymbol{x}_{\rm pk} - \boldsymbol{x}_{\rm gp}) \cdot \boldsymbol{s}_{\rm pk}}{|\boldsymbol{x}_{\rm pk} - \boldsymbol{x}_{\rm gp}|\,|\boldsymbol{s}_{\rm pk}|}.$$

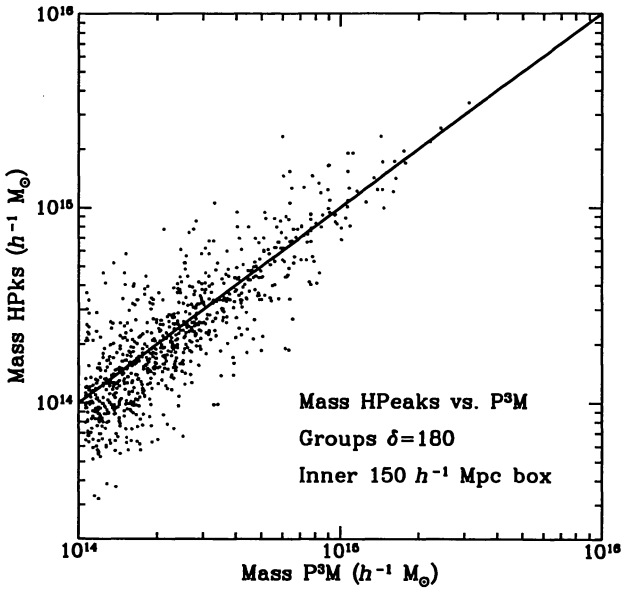

FIG. 10.—Mass of the peak that is paired with a nearby P^{3}M group against the group mass. The peak-patch catalog was constructed for F-peaks with threshold $f_t = 1.686$, using ellipsoidal dynamics and binary reduction. The groups were found using the SPO method with $\delta_{V\rm cut} = 180$. The peak paired with a given group is the nearest one in mass and position to the group, as described in the text. There are 745 distinct peaks matched with 836 groups, with a mass deviation of $\langle \delta \log M_{\rm pk-gp} \rangle = -0.034 \pm 0.186$ ($-7.5\% \pm 53.5\%$).

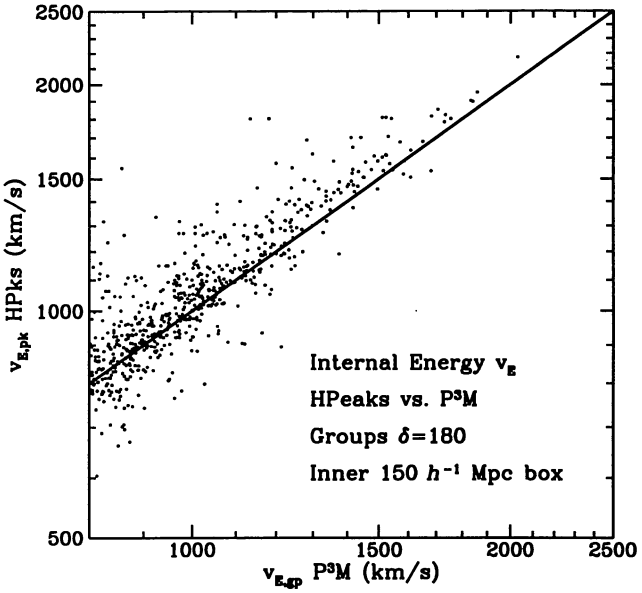

FIG. 11.—The velocity dispersion $v_{E,pk}$ estimated from peak-patch internal energy for the paired peak is plotted against $v_{E,gp}$ of the corresponding group. There are 745 distinct peaks matched with 836 groups, with a velocity deviation $\langle \delta \log v_{E,pk-gp} \rangle = 0.020 \pm 0.055$ (+4.7% ± 13.5%).

For peaks matched with $M_{gp} \geq 2.106 \times 10^{14}\, h^{-1}\, M_\odot$ groups, we find

$$\langle \mu_{V,pk-gp} \rangle = 0.873 \pm 0.213, \quad \langle \mu_{\delta V,pk-gp} \rangle = 0.040 \pm 0.600, \quad \langle \mu_{\delta S,pk-gp} \rangle = 0.041 \pm 0.574 .$$

Thus, the velocity vectors are aligned to $\cos^{-1} \langle \delta\mu \rangle = 29°$ on average. However, we find that the velocity and position residuals are roughly randomly distributed with respect to the peak velocity and displacement vector: the projected components are

$$\langle (x_{pk} - x_{gp}) \cdot \hat{s}_{pk} / |s_{pk}| \rangle = 0.016 \pm 0.333 ,$$

$$\langle (V_{P,pk} - V_{P,gp}) \cdot \hat{V}_{P,pk} / |V_{P,pk}| \rangle = -0.037 \pm 0.449 ,$$

i.e., a small correction in the mean for both positions and velocities along the peak displacement vector direction. For these peaks the mean linear displacement and standard deviation about the mean was $\langle |s_{pk}| \rangle = 5.2 \pm 2.3\, h^{-1}$ Mpc and the mean linear speed was $\langle |V_{P,pk}| \rangle = 525 \pm 227$ km s^{-1}.

The magnitudes of the position, peculiar velocity and speed residuals relative to the peak values are

$$\langle |x_{pk} - x_{gp}| / |s_{pk}| \rangle = 0.472 \pm 0.406 ,$$

$$\langle |V_{P,pk} - V_{P,gp}| / |V_{P,pk}| \rangle = 0.599 \pm 0.544 ,$$

$$\langle (|V_{P,pk}| - |V_{P,gp}|) / |V_{P,pk}| \rangle = -0.208 \pm 0.517 .$$

Another way of expressing this is to compare the absolute residuals

$$\langle |V_{P,pk} - V_{P,gp}| \rangle = 266 \pm 185 \text{ km s}^{-1} ,$$

$$\langle |V_{P,pk}| - |V_{P,gp}| \rangle = -74 \pm 190 \text{ km s}^{-1}$$

with 525 ± 227 km s^{-1} or with the rms velocity for the $\sigma_8 = 0.97$ CDM model, 730 km s^{-1} for a sharp k-space filter of $k^{-1} \approx 4\, h^{-1}$ Mpc. Thus, the peak speeds are ~21% lower than the corresponding group speeds, and the mean velocity and position differences are around 60% and 50% of the peak peculiar velocity and displacement, respectively.

To get a better feel for the correspondences for the best matches and highest masses, we repeat the exercise with higher mass groups: $M_{gp} \geq 5 \times 10^{14}\, h^{-1}\, M_\odot$ and matching peaks with $\delta r_{max} = 2\, h^{-1}$ Mpc, $\delta \log M_{max} = 0.3$ normalized at $\delta r_0 = 0.5\, h^{-1}$ Mpc and $\delta \log M_0 = 0.1$. In the inner 150 h^{-1} Mpc of the box we match 79 peaks to 79 groups out of the total of 125 groups meeting the selection criteria. There will be no problem with duplicate matching. For these matches,

$$\langle \mu_{V,\mathrm{pk-gp}} \rangle = 0.900 \pm 0.177, \quad \langle \mu_{\delta V,\mathrm{pk-gp}} \rangle = 0.220 \pm 0.558, \quad \langle \mu_{\delta S,\mathrm{pk-gp}} \rangle = 0.031 \pm 0.524.$$

Although there is still no orientation preference between the position differences and the peak displacement vector, there is a small component of the velocity difference along the peak velocity,

$$\langle (\boldsymbol{x}_{\mathrm{pk}} - \boldsymbol{x}_{\mathrm{gp}}) \cdot \hat{\boldsymbol{s}}_{\mathrm{pk}} / |\boldsymbol{s}_{\mathrm{pk}}| \rangle = -0.011 \pm 0.255,$$

$$\langle (\boldsymbol{V}_{P,\mathrm{pk}} - \boldsymbol{V}_{P,\mathrm{gp}}) \cdot \hat{\boldsymbol{V}}_{P,\mathrm{pk}} / |\boldsymbol{V}_{P,\mathrm{pk}}| \rangle = -0.148 \pm 0.463,$$

$$\langle (|\boldsymbol{V}_{P,\mathrm{pk}}| - |\boldsymbol{V}_{P,\mathrm{gp}}|) / |\boldsymbol{V}_{P,\mathrm{pk}}| \rangle = -0.292 \pm 0.523.$$

The velocity correction in the peak velocity direction is 15% while the mean difference in peak and group speeds is nearly twice that. For these higher mass peaks, $\langle |\boldsymbol{s}_{\mathrm{pk}}| \rangle = 4.3 \pm 1.8\ h^{-1}$ Mpc and $\langle |\boldsymbol{V}_{P,\mathrm{pk}}| \rangle = 433 \pm 177$ km s^{-1}.

We conclude that for this CDM model, peak positions using linear displacements give quite reasonable agreement with the group positions. This is what one also infers visually from the direct-comparison figures. For the velocities, a correction in both direction and amplitude to the linear velocity is necessary. Although for this CDM model, the correction vector has, on average, a significant projection along the direction of the linear velocity, there is also a sizable perpendicular component. Both contribute to the discrepency in the speeds, which conspires to make the linear velocities ~20% too low relative to the true group velocities. In BM4, we adopted a rough correction factor to the linear velocities based upon assuming quadratic nonlinearities dominate:

$$f^{\mathrm{nl}} = F_\nu (1 - 3e_v^2 - p_v^2)/14, \tag{3.10a}$$

$$\boldsymbol{s}^{\mathrm{nl}} = f^{\mathrm{nl}} \boldsymbol{s}, \qquad \boldsymbol{V}^{\mathrm{nl}}_{P,\mathrm{pk}} = 2 f^{\mathrm{nl}} \boldsymbol{V}_{P,\mathrm{pk}}, \tag{3.10b}$$

$$\boldsymbol{s}^{\mathrm{cor}} = \boldsymbol{s} + \boldsymbol{s}^{\mathrm{nl}}, \qquad \boldsymbol{V}^{\mathrm{cor}}_{P,\mathrm{pk}} = \boldsymbol{V}_{P,\mathrm{pk}} + \boldsymbol{V}^{\mathrm{nl}}_{P,\mathrm{pk}}. \tag{3.10c}$$

Although we showed that the nature of the correction was not a simple amplification of the linear displacement and velocity vectors, that assumption is the simplest to implement and gives an idea of the magnitude of the nonlinear correction we should expect. For our matched high-mass peaks, we have

$$\langle |f^{\mathrm{nl}}| \rangle = 0.121 \pm 0.004,$$

$$\langle |\boldsymbol{s}^{\mathrm{nl}}| \rangle = 0.52 \pm 0.20\ h^{-1}\ \mathrm{Mpc},$$

$$\langle |\boldsymbol{V}^{\mathrm{nl}}_{P,\mathrm{pk}}| \rangle = 103 \pm 40\ \mathrm{km\ s^{-1}},$$

in line with the 29% difference in speeds found from the linear peaks versus P^{3}M groups. However, we find that the alignment assumption gives a net component of the relative Eulerian positions along the displacement direction, which is not seen if we just use the linear displacements for the peaks.

Thus, if we are to use peak patches in catalog construction, provided we are interested only in locations, we can just use the Zeldovich approximation. However, if bulk velocities are of direct interest, they should be corrected. The statistics of the residuals do not reveal a simple prescription for this nonlinear correction. Our rough quadratic approximation does give the correct speed distribution on average. For example, the top 100, 400, and 2000 groups (in mass) have rms velocities of 638, 693, and 717 km s^{-1}, respectively; for peaks with linear velocities, we get 508, 550, and 619 km s^{-1}, and when the aligned quadratic correction (with $\theta = 1$) is included, we get 630, 682, and 765 km s^{-1}. A nonlinear correction to the peak peculiar velocities along the velocity vector is therefore mandated by the detailed comparison with N-body, although there is no such indication for a displacement correction.

3.4. *Spatial Distribution of Groups and Peak Patches*

In § 3.3, we saw that the mean distance from a group to its paired peak is 2.0 h^{-1} Mpc for groups with $M_g \geq 2.1 \times 10^{14}$ h^{-1} $M_\odot$. We now examine in more detail the spatial correspondence between the P^{3}M groups and peaks. For example, Figures 12 and 13 show the (x, y) projections of the positions of the P^{3}M particles belonging to the groups (with $E_{\mathrm{int}} < 0$, i.e., internally bound) above a mass cut corresponding to 400 P^{3}M particles, $M_g \geq 4.21 \times 10^{14}\ h^{-1}\ M_\odot$. There were 380 P^{3}M groups above this cut. Only the inner $(150\ h^{-1}\ \mathrm{Mpc})^3$ region of the box is shown, in which there are 163 groups.

The peaks are shown at their final Eulerian positions after the Zeldovich approximation transport. A Lagrangian sphere of radius R_{pk} would compact into one of size $R_{\mathrm{E,pk}} = 0.3 R_{\mathrm{pk}}/F_{\mathrm{pk}}$ if its density were constant (top-hat profile). For $F_{\mathrm{pk}} = 1.686$, this is 0.177 R_{pk}, which is just $R_{\mathrm{pk}}/(1 + \delta_{V\mathrm{cut}})^{1/3}$, with $\delta_{V\mathrm{cut}} \approx 180$. This is the radius of the spheres shown in the figure. The arrows show where the peak patch originated in Lagrangian space. The figures illustrate how the different ways of selecting candidate peaks affects the spatial comparison: In Figure 12, 163 groups are plotted, along with their 153 paired peak partners. In Figure 13*a*, we add a few more lower mass peaks (rank-ordered in mass) to bring the number in the full box up to 380, the same as the number of groups in

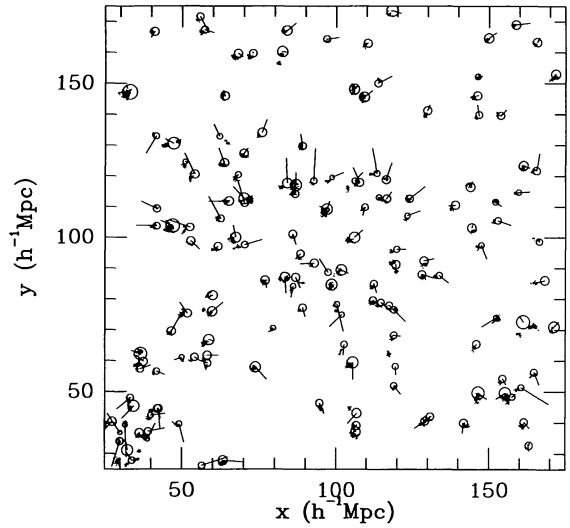

FIG. 12.—x, y projection of the peaks and P^{3}M groups in the inner 150 h^{-1} Mpc of the 200 h^{-1} Mpc box. One in 5 particles from the ($\delta_{Vcut} = 180$) P^{3}M groups with $M_g \geq 4.21 \times 10^{14}\ h^{-1}\ M_\odot$ are shown. A threshold $f_t = 1.686$, ellipsoidal dynamics and binary reduction was used for the peaks. The peaks matched to the P^3M groups are those nearest in space and mass, as described in the text; this paired 357 peaks to the 380 groups in the full 200 h^{-1} Mpc box. The peaks are shown in their Eulerian positions as circles, with radii equal to the Eulerian "final" top-hat radius $R_{E,pk} = 0.177 a_{pk} R_{pk}$, and the vectors show the displacements from the initial Lagrangian positions.

the entire box, which extended the mass range down to $M_p \geq 4.00 \times 10^{14}\ h^{-1}\ M_\odot$ for the peaks. In Figure 13*b*, we plot the top F peaks for the threshold $f_t = 0.01$. In Figure 13*c* and 13*d*, the λ_{v3} peaks and λ_{v1} peaks (with F threshold $f_t = 0.01$) are shown, respectively. Once again, the F peaks seem to do a little better compared with the N-body groups than the shear tensor eigenvalues, although they all seem to get the high masses right.

Visually, the spatial correspondence of the paired peaks with the N-body groups is very good, in spite of the Zeldovich moving. The most noticeable differences are in the merging of close groups and peaks, for which we might expect counting problems; these also lead to problems in matching peak-patch properties with those of the groups. The peaks with the same mass cut or same number also show good visual correspondence to groups, even though there are errors due to the scatter in the peaks P^{3}M mass relation at the cutoff.

In Figures 14*a*–14*b*, we give a three-dimensional impression of the Eulerian-space correspondence, by showing the (x, y, z) comoving positions of the groups and peaks with the same $4 \times 10^{14}\ h^{-1}\ M_\odot$ mass cut, within the inner (100 h^{-1} Mpc)^3 of the box. Showing the three-dimensional correspondence in (initial) Lagrangian space is more awkward because so much of the space is taken up by the higher mass objects. We attempt to do this in Figures 15*a*–15*b*. We show a very narrow 10% mass range centered around $5 \times 10^{14}\ h^{-1}\ M_\odot$ for the groups (those with 450–500 particles). The paired peak patches have spheres of radius R_{pk} plotted. Even though Eulerian space matching was done, the visual correspondence in Lagrangian space is good. Note that the Lagrangian patches that collapse to form the groups are quite compact and relatively spherical.

We conclude that the correspondence between the hierarchical peaks and the P^{3}M groups is remarkably good, considering the number of simplifying approximations made during the formulation of the algorithm. There is a larger than desirable scatter in the individual mass and velocity dispersions of the peaks with respect to the N-body groups, but the spatial correspondence between peak and group is really very good at the high-mass end. Also, the agreement between the peak and group mass functions and number-velocity dispersion counts is very good. We also showed that the Press-Schechter mass function can be simply adjusted to fit the P^{3}M data, which gives renewed confidence in the viability of that vast array of papers that use it.

4. DISCUSSION AND CONCLUSIONS

In this paper, we have validated the peak-patch code with an N-body code. We find our hierarchical peaks method accords extremely well with Couchman N-body groups in position, mass, internal energy, and number density for high-mass peaks, but with growing scatter for lower mass objects.

We decided that the standard friends-of-friends approach to group finding was inadequate, since the translation of the percolation parameter p into a volume-averaged overdensity is very rough. Our new group finder is based upon (1) adaptive smoothing to define continuous fields which the particles sample, (2) searches that begin with high smoothed density peaks of the fields, but with corrector steps to center the group at the center of mass, and (3) truncation once interior overdensity falls below some threshold defined by a group crossing-time criterion. We believe our group membership lists are more physically meaningful than percolation, will be more stable to variation in particle number in the simulations and, when more than one threshold is used, will do better than percolation with multiple linking-parameters in dealing with substructure of recently merged entities.

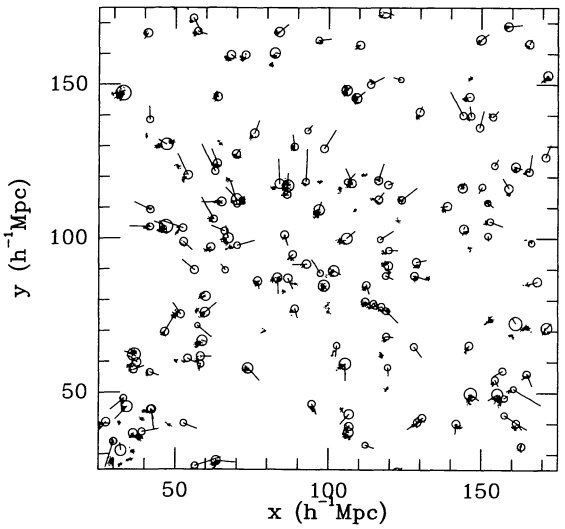

FIG. 13*a*

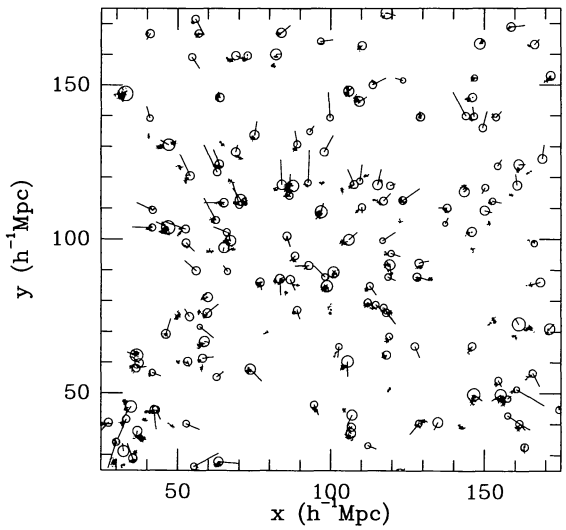

FIG. 13*b*

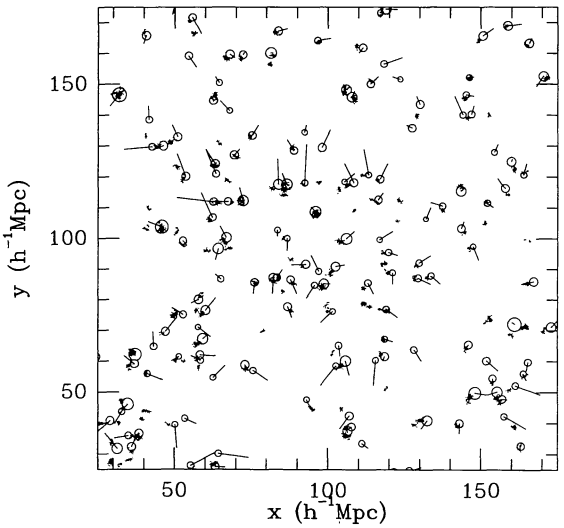

FIG. 13*c*

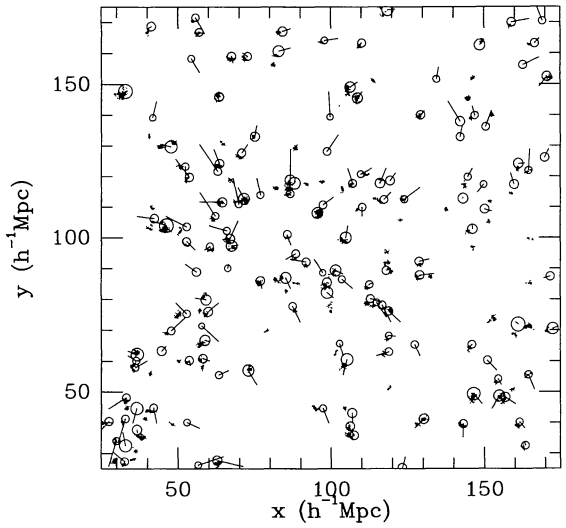

FIG. 13*d*

FIG. 13.—x, y projection of the peaks and P^{3}M groups in the inner 150 h^{-1} Mpc of the 200 h^{-1} Mpc box. One in 5 particles from groups with $M_g \geq 4.21 \times 10^{14}\, h^{-1}\, M_\odot$ are shown (380 groups in the full 200 h^{-1} Mpc box). The peak masses were calculated using ellipsoidal dynamics, overlaps were removed using binary reduction, and the peak mass limit was chosen to give the same number of peaks as P^{3}M groups in the full volume (380). The peaks are shown in their Eulerian positions as circles, with radii equal to the Eulerian "final" top-hat radius $R_{\rm E,pk} = 0.177\bar{a}_{\rm pk} R_{\rm pk}$, and the vectors show the displacements from the initial Lagrangian positions. (*a*) F-peaks above $f_t = 1.686$; (*b*) F-peaks above $f_t = 0.01$; (*c*) λ_{v3} peaks above $f_t = 0.01$; (*d*) λ_{v1} peaks above $f_t = 0.01$.

However, there is no substitute for using more local physics information to define the groups better. Thus, there are a number of alternatives to our basic approach which may be more appropriate, depending upon what we wish our groups to be. For example, we have also tried gravitational potential minima to define the rank-ordered candidate points rather than density, but because of the corrector steps this did not prove to be superior. Instead of volume-average overdensity, defining membership based upon particles which are bound to the group may be superior (e.g., Gelb 1992). However, we find that the groups are often not in isolated virial equilibrium.

Although we showed that infall, external tidal forces, and dynamical activity following recent mergers will modify the virial equation, we have been quite surprised that isolated equilibrium is such a poor approximation for so many of the P^{3}M groups, irrespective of overdensity cut (Fig. 3). We note that P^{3}M codes currently use a spatially uniform time step. The compromise between accurate treatment of internal group dynamics and timely advancement of the entire simulation is usually made by judiciously softening the gravitational force. However, even within the softened gravity theory, computed particle orbits may have little to do with real particle orbits, instead leaping about the group with giant strides because the ticking of the global clock is so

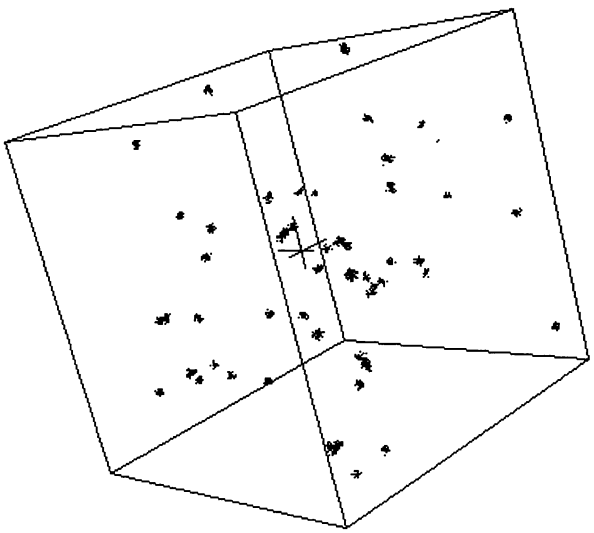

FIG. 14*a*

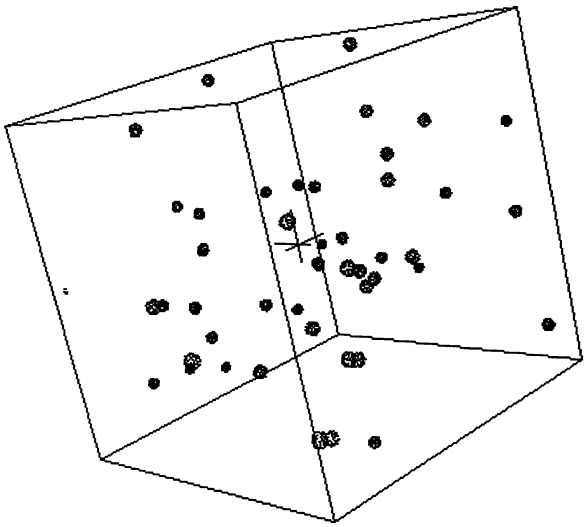

FIG. 14*b*

FIG. 14.—The direct comparison (in Eulerian space) of the *N*-body clusters (determined with our group finder) and the peaks from our simulation. These three-dimensional representations of the cubical simulations cover the central $(100\ h^{-1}\ \mathrm{Mpc})^3$ of the total $(200\ h^{-1}\ \mathrm{Mpc})^3$ volume. (*a*) All $\mathrm{P^3M}$ clusters above $4 \times 10^{14}\ h^{-1}\ M_\odot$ whose centers of mass lie within the volume are included. (*b*) Density peak-patches above $4 \times 10^{14}\ h^{-1}\ M_\odot$, found using $f_t = 1.686$, ellipsoidal dynamics, and binary reduction. The correspondence between the most massive peaks and clusters is excellent. Lower mass peaks and groups suffer from merging and overlap problems, but retain reasonable correspondence as the agreement between the mass functions reveals.

mismatched to the desired ticking of the local clock. A very worthwhile exercise for future work is to thoroughly explore which local group properties are robust and which are not in these big simulations which are invaluable for building large statistical samples. We believe that emphasizing the measurement of conserved or approximately conserved quantities is ideal. (We note that a non-adaptive *PM* calculation of a region the size of the $\mathrm{P^3M}$ calculation kindly provided by Jens Villumsen at an early stage of this work had groups that had smaller kinetic energies and that were less compact than the $\mathrm{P^3M}$ groups, both not surprising. We also note that both the tree and multigrid Gauss-Seidel calculations of the constrained field for a single low-mass cluster described in BM1, which

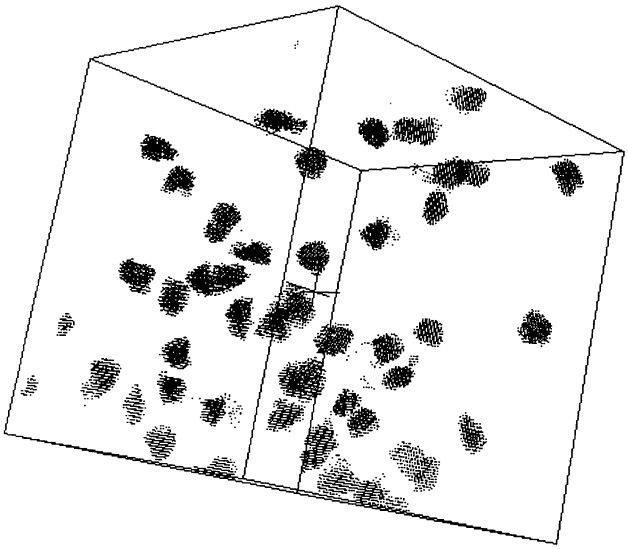

FIG. 15*a*

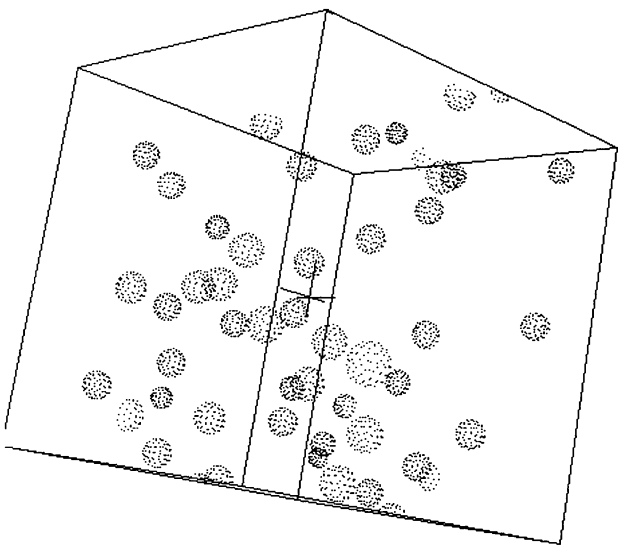

FIG. 15*b*

FIG. 15.—(*a*) 3D positions in Lagrangian (initial) space of particles belonging to *N*-body clusters in the mass range $(4.75\text{–}5.25) \times 10^{14}\ h^{-1}\ M_\odot$ (found with our group finder using a volume-averaged overdensity cut of 180). The three-dimensional cube covers the full $(200\ h^{-1}\ \mathrm{Mpc})^3$ of the simulation. (*b*) Hierarchical peak-patches nearest in Eulerian (final) space to the clusters in (*a*) (and of comparable mass) are shown. (The apparently nonassociated points are joined through the periodic boundary conditions.) This shows that the regions of Lagrangian space that form the interior of these clusters (which are not that rare in a $\sigma_8 = 0.97$ model) are not very aspherical.

were of higher resolution than the P^{3}M simulation described here, gave better isolated equilibrium results, although the major merger just prior to the predicted cluster assembling time did upset equilibrium.)

A by-product of our analysis is another demonstration that the Press-Schechter mass function, if treated phenomenologically, gives a remarkably accurate representation of the N-body group mass function, if we treat f_c as a parameter to be fit. Prior testing of the Press-Schechter paradigm with N-body results was done by Efstathiou et al. (1988), Narayan & White (1987), Efstathiou & Rees (1988), Carlberg & Couchman (1989), Bond et al. (1991), and Gelb (1992). White et al. (1992) have also recently tested the mass function for a simulation as large as the one used here. Our results confirm the remarkable success story of the Press-Schechter formula, except that we should either lower the density threshold f_c by $\sim$6% or increase the masses by $\sim$30%. A slightly smaller decrease in f_c would be needed to fit $p = 0.2$ percolation groups (which is what Bond et al. [1991] used to test the PS and other excursion set mass functions). We also showed that the internal energy function can be reproduced with a relation $v_E \approx 1.59HaR_{TH}(1 + z_c)^{1/2}$, where z_c is the redshift in question, for $\Omega_{nr} = 1$ models. The kinetic energy function requires $v_K \approx 1.9HaR_{TH}(1 + z_c)^{1/2}$. However, we recall from Bond et al. (1991) that the Press-Schechter mass function calculation really has no theoretical justification. To defend its use, we would now say: *use of the* PS *formula is justified because it fits the hierarchical peak-patch function with ellipsoidal dynamics so well.* Certainly why the rare-event tail does well can be understood in this context. The reader may judge whether this is better than: use of the PS formula is justified because it fits N-body groups so well. Neither justification extends to the low-mass slope, however.

Prior testing of the peaks paradigm was very limited, and, in any case, used single-filter peaks. Gelb, Katz, & Quinn (1993) announced that peaks are *not* the sites of galaxy formation, using a large N-body simulation for testing, but they also only used single-filter peaks. We would certainly like to compare the hierarchical peaks method in detail with the results of a large N-body simulation for a flatter spectrum than the CDM model in the group-to-cluster waveband gives (spectral slope varying from about -1.5 up to 0). For flatter spectra, e.g., the CDM model over the wavebands appropriate for galaxy formation (spectral slope varying from about -2.5 up to -1.5), there is a larger mismatch between the coherence of the displacement field and the structure in the density field. Thus one may get large Zeldovich transport, since the adaptive smoothing associated with the peak's radius would not diminish much the power in the bulk velocity spectrum. This is not a problem, however, because the flow is very coherent, and it is the deviations from smooth flow which determines how objects come together. However, the deviations often lead to the formation of large-scale filamentary structure. Through such anisotropies, it may be possible for long-wavelength components of the fields to bring two distant peaks together without having a large-scale spherical peak with an overdensity above threshold encompassing the two sublumps. It could therefore be that the spherical peak-patch description might need some modifications: for example, one might consider ellipsoids in Lagrangian space instead of spheres; final state merging, which we have implemented but found to be unimportant so far, might also be useful in such cases. We do not know yet if the success of the peak-patch approach in reproducing the spatial distribution will be as great for galaxy formation. We have little doubt that the high-mass rare halos will be adequately described. In BM4, we show that the peak-patch mass functions for power low initial conditions with $n = 0, -1, -2$ are in good accord with the group mass functions.

What is essential to the hierarchical peak-patch picture is that the patches be *just* collapsed to ensure that the region outside of the patches is not too dynamically active. What it cannot answer in detail is galaxy merging within groups long after the galaxies have formed and issues associated with how baryonic dissipation breaks the hierarchy. External criteria for these would have to be added to the theory just like they have to be added to N-body simulations. What one can use for merging within a hierarchical peak patch identified at redshift 0, say, is the peak patches within it that are excluded at $z = 0$, but which survive as hierarchical peaks at higher redshift. That is, we would determine radii and internal properties as a function of a sequence of collapse redshifts. This adds almost no extra computational cost, just a little extra storage. In this sense, having clouds in clouds is advantageous.

A much more sophisticated treatment of the left over bits of Lagrangian space is needed to develop a theory of small-mass objects, and, in particular, the faint-end slope of the mass function. Tiny peaks are very sensitive to local tidal fields: we showed in § 2 that a number of the small peaks do not lead to collapses when we include the effects of shear fields even though their density contrast is above the threshold $f_t = 1.686$. Of course, N-body groups with only tens of particles are also quite sensitive to the specific algorithm used to find them.

The hierarchical peak-patch paradigm has an analytic counterpart which is almost as easy to implement as the single filter peak model of BBKS, but is *much* more physical and richer, because now the mass hierarchy can be described. Throughout BM1 and this paper, we have plotted analytic curves for mass, velocity dispersion, and bulk velocity distribution functions, and for the mass-radius and mass-velocity relations and shown that they give highly accurate results compared with our Monte Carlo catalogs. Just as the Monte Carlo method is a few orders of magnitude faster than P^{3}M calculations, so the analytic methods gain similar speedup factors over the Monte Carlo calculations. We present the analytic and semi-analytic aspects in BM4.

The ability to calculate statistical correlations induced by biasing was one of the most important successes of the BBKS theory. In the BBKS theory, this can be done directly or by means of a "peak-background split," in which intermediate waves define the structure of the peaks and long waves determine a modulating background. Bond & Couchman (1987, 1989) showed how to include Zeldovich dynamics within the peak-background split semi-analytically. In this paper, our comparisons have focussed on one-point functions and detailed peak-to-group correspondences, but the latter suggests that two-point correlation functions should also compare favorably, with the caveat that overmerging or undermerging can affect the correlations. We report on correlations in BM4, where we show that analytical calculations using a modification of the "peak-background split" still works. The Bond & Couchman method for including Zeldovich dynamics also works. However, we show in BM4 that the bias factors one computes based upon a cut in density of clusters differ from those obtained in single filter theory.

We thank Hugh Couchman for providing his CDM simulation for us to compare our method with, and for many discussions on its use. This research was supported by the NSERC of Canada at CITA and by the NSF at Caltech. J. R. B. was supported by a Canadian Institute for Advanced Research Fellowship.

APPENDIX
SMOOTHED-PARTICLE OVERDENSITY GROUP-FINDING

For our group-finding algorithm, we need to calculate a volume-averaged overdensity, $1 + \langle\delta\rangle_V = (M_{\rm gp}/V_{\rm gp})/\bar{\rho}_{\rm nr}$, where now $\bar{\rho}_{\rm nr}$ denotes the cosmological background density (in nonrelativistic particles) rather than the mean density in the simulation volume. We therefore need to calculate the volume for regions that may have funny shape. We also need to find a particle that lies within one of these high-density contrast regions. We first calculate a smoothed density for each particle. To do this, we use an adaptive spherical spline to do the smoothing. In particular, we choose the window function $W_{\rm sph}$ (given in BM1 § 2.2.1), with a different filter scale h_p for each particle p. To get h_p, we require that N_h particles are contained within a sphere of radius $2h_p$ centered at particle p. We choose $N_h = 32$ for the results shown here.

The smoothing kernel $W_{\rm sph}$ is used to interpolate the smooth density field onto the particles. We assign a density

$$\rho_p = \sum_{p'=1}^{N} m_{p'} W_{\rm sph}(\boldsymbol{x}_p - \boldsymbol{x}_{p'}; h_p) \tag{A1}$$

to each particle. To estimate the volume V, we write

$$V = \int \frac{dm}{\rho} = \sum_{p=1}^{N} \frac{m_p}{\rho_p} \int_V d^3\boldsymbol{x} W_{\rm sph}(\boldsymbol{x} - \boldsymbol{x}_p; h_p) \approx \sum_{\text{for } p \text{ inside}} \frac{m_p}{\rho_p}. \tag{A2}$$

The final sum is over particles that are inside the region. Thus, in effect, each particle is carrying with it a smoothed volume element $V_p = m_p/\rho_p$. We store the quantities h_p and ρ_p in the particle file along with the particle information $\boldsymbol{x}_p$, v_p, and m_p. Because the group overdensity is determined using locally adaptive smoothing, we also refer to this method as the "smoothed particle overdensity" (SPO) group-finder.

To make a candidate list of group starting points, we begin by making a target list of those particles with $\delta_p \geq \delta_{V\,\rm cut}$. We rank these in decreasing order of density. The first group begins with the highest density particle (the test particle). From the full list of particles not already in groups, neighboring particles within some chosen outer distance are selected using a tree-search algorithm, and ranked in increasing distance from the central test particle. Particles are added to the group in distance order. The volume-averaged overdensity for the volume out to the position of the most recent particle p included is tallied:

$$\langle\delta\rangle_V(<p) = \frac{1}{\bar{\rho}_0 V(<p)} \sum_{p' \text{ inside } p} m_{p'}, \qquad \text{where } V(<p) \equiv \sum_{p' \text{ inside } p} \frac{m_{p'}}{\rho_{p'}}. \tag{A3}$$

When the group overdensity $\langle\delta\rangle_V(<p)$ reaches the desired critical overdensity $\delta_{V\rm cut}$, the search is ended and the ranked particles up to p are assigned to the group. However, the highest density point we began with is not necessarily the best center for the membership determination. To remedy this we take a sequence of corrector steps. We determine the center of mass $\boldsymbol{x}_{\rm cm}$ for the group. We then repeat the group procedure with $\boldsymbol{x}_{\rm cm}$ the new center of the search. We continue to loop through group membership determination until the shift in the center stabilizes below some chosen tolerance. The iterations are stopped and the final group membership list is written out.

We now go to the next highest density particle in the target list not already spoken for by a prior group and repeat the procedure. And of course we do not allow particles to belong to more than one group. We repeat until the target list is exhausted.

Note that although we go out from the center in distance order, this does not mean that we are making a spherical approximation. The group can be arbitrarily lumpy in density. There can be directions with few or no particles. The corrector steps are designed to ensure that the high-density clump we begin with does not just happen to be on the outskirts of most of the mass in the group. We can also imagine many modifications of the algorithm which fold in directional asymmetry in the steps. The crucial thing to ensure is that when a particle is added, the "smooth-particle" volume it adds is connected to the growing volume. The easiest way to ensure that is to work out in distance order from a center. We have checked that the sizes we get by this volume determination method agree with those obtained by simpler ellipsoid fitting methods as the group grows.

For the n_g particles p in each group g we compute the total mass M_g, the center of mass position $\boldsymbol{x}_g$, the top-hat equivalent radius R_g, the mass quadrupole tensor Q_{ij}, the average group peculiar velocity $\boldsymbol{V}_{Pg}$, and the angular momentum vector $\boldsymbol{J}$:

$$M_g = \sum_{p=1}^{n_g} m_p, \qquad \boldsymbol{x}_g = \frac{1}{M_g}\sum_{p=1}^{n_g} m_p \boldsymbol{x}_p,$$

$$R_g = \left(\frac{3}{4\pi}\sum_{p=1}^{n_g}\frac{m_p}{\rho_p}\right)^{1/3}, \qquad Q_{ij} = \frac{1}{M_g}\sum_{p=1}^{n_g} m_p \bar{a}^2 (\boldsymbol{x}_p - \boldsymbol{x}_g)_i (\boldsymbol{x}_p - \boldsymbol{x}_g)_j ,$$

$$\boldsymbol{V}_{Pg} = \frac{1}{M_g}\sum_{p=1}^{n_g} m_p \boldsymbol{V}_{Pp}, \qquad \bar{\boldsymbol{J}} = \frac{1}{M_g}\sum_{p=1}^{n_g} m_p \bar{a}(\boldsymbol{x}_p - \boldsymbol{x}_g) \times (\boldsymbol{v}_p - \boldsymbol{v}_g) .$$

where $\boldsymbol{v} = H\bar{a}\boldsymbol{x} + \boldsymbol{V}_P$ is the total velocity. The background scale factor $\bar{a}$ enters because the positions are comoving ones.

REFERENCES

Bardeen, J. M., Bond, J. R., Kaiser, N., & Szalay, A. S. 1986, ApJ, 304, 15 (BBKS)

Binney, J., & Tremaine, S. 1987, Galactic Dynamics (Princeton: Princeton Univ. Press

Bond, J. R. 1989, in Frontiers of Physics—From Colliders to Cosmology, ed. A. Astbury et al. (Singapore: World Scientific), 182

Bond, J. R., Cole, S., Efstathiou, G., & Kaiser, N. 1991, ApJ, 379, 440

Bond, J. R., & Couchman, H. M. P. 1987, in Proc. 2d Canadian Conf. on General Relativity & Relativistic Astrophysics, ed. A. Coley, C. Dyer, & B. Tupper (Singapore: World Scientific), 289

———. 1989, Large-Scale Structure & Motions in the Universe, ed. G. Giuricin, F. Mardirossian, M. Mezzetti, M. Ramella (Dordrecht: Kluwer), 335

Bond, J. R., & Myers, S. 1995a (BM1), ApJS, 103, 1

———. 1995b, ApJS, 103, 63 (BM3)

———. 1995c, (BM4) preprint

Carlberg, R. G., & Couchman, H. M. P. 1989, ApJ, 340, 47

Couchman, H. M. P. 1991, ApJ, 368, L23

Efstathiou, G., Frenk, C. S., White, S. D. M., & Davis, M. 1988, MNRAS, 235, 715

Efstathiou, G., & Rees, M. 1988, MNRAS, 230, 5P

Evrard, G. 1990, ApJ, 363, 349

Frenk, C. S., White, S. D. M., Efstathiou, G., & Davis, M. 1990, ApJ, 351, 10

Gelb, J. 1992, Ph.D. thesis, MIT

Gelb, J., Katz, N., & Quinn, T. 1993, MNRAS, 265, 689

Narayan, R. & White, S. D. M. 1987, MNRAS, 231, 97P

White, S. D. M., Efstathiou, G., & Frenk, C. S. 1993, MNRAS, 262, 1023